

UC Merced

UC Merced Electronic Theses and Dissertations

Title

Design of magnetic and semiconducting nanoparticles assembled in a liquid crystalline matrix as sensors for magnetic fields and multi-scale investigations to improve post-situ control to progress toward fluid-based processing

Permalink

<https://escholarship.org/uc/item/6z55w45b>

Author

Amaral, Jose Jussi

Publication Date

2018

Copyright Information

This work is made available under the terms of a Creative Commons Attribution License, available at <https://creativecommons.org/licenses/by/4.0/>

Peer reviewed|Thesis/dissertation

UNIVERSITY OF CALIFORNIA, MERCED

Design of magnetic and semiconducting nanoparticles assembled in a liquid crystalline matrix as sensors for magnetic fields and multi-scale investigations to improve post-situ control to progress toward fluid-based processing

A dissertation submitted in the partial satisfaction
of the requirements for the degree of

Doctor of Philosophy
in
Physics

by
Jose Jussi Amaral

Committee in Charge
Professor Linda S. Hirst, Chair
Professor Vincent Tung
Professor Sayantani Ghosh, Principal Investigator

2017

Chapter 3 © 2016 IOPscience
Chapter 4 © 2015 The Royal Society of Chemistry
All other chapters © 2017 Jose Jussi Amaral

The dissertation of Jose Jussi Amaral is approved, and it is acceptable in quality and form for publication on microfilm and electronically:

Syantani Ghosh

Vincent Tung

Linda S. Hirst (Chair)

University of California, Merced

2017

To Andrea. Talking physics at the end of the day with her was the highlight of my journey through graduate school. She is a force to be reckoned with.

To my parents. I am so thankful for everything they taught me, and helped me learn. My mother for strength and unwavering support, and my father because I wanted to follow in his footsteps.

To our dogs. Because of them, no day was a bad day.

Contents

I Curriculum Vitae	vi
II Abstract of the Dissertation	1
1 Introduction	3
1.1 Nanoparticles	3
1.1.1 Quantum Dots	3
1.1.2 Magnetic Nanoparticles	6
1.2 Liquid Crystalline Materials	7
1.3 Motivation	8
2 Magneto-optical Kerr Effect Microscopy	11
2.1 Magneto-optical Kerr Effect	11
2.2 Optical Setup	11
2.3 Experimental Data	12
3 Effect of mesogenic ligands on short and long-term spectral dynamics and stability of core-shell CdSe/ZnS quantum dots	13
3.1 Introduction	13
3.2 Experimental details	13
3.3 Results and Discussion	15
3.4 Conclusion	20
4 Magnetic field induced brightening in liquid crystal synergized magnetic and semiconducting nanoparticle composite assemblies	22
4.1 Introduction	22
4.2 Results and Discussion	23
4.2.1 Assembly and structural characterization of nano-composites	23
4.2.2 Synergistic emission enhancement in nano-composites	24
4.2.3 Systematic and reversible optical magnetic sensing	26
4.3 Conclusions	29
4.4 Materials and Methods	29
5 Generating ring-like structures of nanoparticles and nano-scale investigation of magnetic nanoparticle rotation leading to enhanced local magnetization	31
5.1 Introduction	31
5.2 Experimental	31
5.2.1 Nanoparticle co-assembly preparation	31
5.2.2 Ring-like nanoparticle co-assembly preparation	32
5.2.3 Experimental methods	32
5.3 Results and Discussion	32
5.3.1 Assembly and structural imaging of nano-composites	31
5.3.2 Assembly of ring-like microstructures	35
5.3.3 Synergistic emission enhancement in nano-composites	37
5.3.4 Magnetic nanoparticle rotation at the nano-scale	38
5.4 Conclusion	41
6 Conclusion	43
References	44

Curriculum Vitae

Jose Jussi Amaral

Ph.D Candidate

Home Address

134 W Vassar Ave
Fresno, CA 93705

Phone: (559) 790-5451
jamaral2@ucmerced.edu

Work Address

University of California, Merced
5200 North Lake Rd.
S&E Bldg., Rm 371
Merced, CA 95343

Current research interests

- Magneto-optical and polarized microscopy of magnetic and semiconducting nanoparticles in soft matter
- Transmission electron microscopy, Lorentz TEM of nanoparticle rotation

Education

University of California, Merced, Merced, CA Sept. 2011 – In Progress
Fall 2011 (GPA = 3.508/4.0; 4.0 = A) Exp. Graduation Fall 2017
Advisors: Assoc. Prof. Sayantani Ghosh, Physics Department

California State University, Fresno, Fresno, CA Sept. 2009 – 2011
August 2009 to Fall 2011 (GPA = 3.26/4.0; 4.0 = A)
Advisor: Prof. Pei-chun Ho, Physics Department

California State University, Fresno, Fresno, CA Sept. 2006 – June 2008
B.S. in Physics, Dec. 2008 (GPA = 3.14/4.0; 4.0 = A)

Work experience summary

University of California, Merced, Merced CA, Summer 2011 – 2017
Teachers Assistant
Taught Physics 9, 19, Physics 8 , Math 5

California State University, Fresno, Fresno CA 2009-2011
Teachers Assistant
Taught 4 Intro Level Physics classes for non-majors: Phys 10, Phys 2A, Phys 2B, and Nat. Sci 1A

Recognition and honors

1. President's Dissertation Year Fellowship. Academic Year 2015-2016
2. Fletcher-Jones Fellowship. Academic Year 2014-2015
3. Dean's Distinguished Fellowship. Spring 2014
4. Outstanding Science Project. Graduate Research Symposium at CSUF March 2011. Awarding Institution: CSUF and American Chemical Society.
5. Margaret Burbidge Award, 2nd Place, Graduate Experiment. California October American Physical Society Meeting 2010. Awarding Institution: American Physical Society

Invited Talks

1. "Hybrid soft matter materials: all-optical magnetic field sensor & surface modification of quantum dots." J. Amaral. Presentation at the California State University, Fresno Physics Colloquium. Fresno, CA. March 4th, 2016.
2. "Designing Responsive and Synergistic Nanoparticle Assemblies in Liquid Crystal." J. Amaral. Presentation at the XLIV Winter Meeting on Statistical Physics. Mexico City, DF, Mexico, January, 2015.

Publications

1. Jose Jussi Amaral, E. Betady, M. T Quint, D. Martin, S. T. Riahinasab, L. S Hirst and Sayantani Ghosh, "Effect of mesogenic ligands on short and long-term spectral dynamics and stability of core-shell CdSe/ZnS quantum dots," *Materials Research Express*, **3** (10), 2016.
2. Jose Jussi Amaral, A. L. Rodarte, J. Wan, C. Ferri, R. Pandolfi, L. S. Hirst, S. Ghosh, "Magnetic field induced quantum dot brightening in liquid crystal synergized magnetic and semiconducting nanoparticle composite assemblies," *Soft Matter*, **11**, 2015.

Conference and workshop presentations

1. "Understanding surface effects of ligand exchanged Quantum Dots," J. Amaral, Presentation at SPIE, San Francisco, CA, February 2016.
1. "Optical magnetic shift of a directed assembly of CdSe/ZnS quantum dots and iron-oxide nanoparticles in soft matter at low magnetic fields," J. Amaral. Presentation at the American Physical Society March Meeting 2014. Denver, CO, March, 2014.
2. "Self-assembly of magnetic nanoparticles in a liquid-crystalline media." J. Amaral. Presentation at the American Physical Society March Meeting 2013. Baltimore, MD March, 2013.
3. "Synthesis and Analysis of Rare Earth Nanoparticles Using an Inverse Micelle Technique with a Sodium Borohydride Reduction." J. Amaral. Presentation to the Graduate Research and Creative Activities Symposium. Fresno, CA May, 2011.
4. "Synthesis and Analysis of Rare Earth Nanoparticles Using an Inverse Micelle Technique with a Sodium Borohydride Reduction." J. Amaral. Presentation to the Central California Student Research Symposium. Fresno, CA April, 2011.
5. "Synthesis and Analysis of Rare Earth Nanoparticles Using an Inverse Micelle Technique with a Sodium Borohydride Reduction." J. Amaral. Poster presentation at the APS March Meeting. Dallas, Tx. March, 2011.
6. "Synthesis and Analysis of Rare Earth Nanoparticles Using an Inverse Micelle Technique with a Sodium Borohydride Reduction." J. Amaral. Presentation to the California-Nevada Annual October APS Meeting 2010. Pasadena, CA October, 2010.
7. Society of Physics Students (SPS) Press Article: APS March Meeting 2011 in Dallas.
http://www.spsnational.org/meetings/reports/2011/aps_march_amaral.htm

8. Carmin Liang, Dulce Romero, Jussi Amaral, Faculty Advisor: Pei-Chun Ho, Acknowledgements: Saeed Attar, Dennis Margosan, "Synthesis and characterization of rare-earth gadolinium nanoparticles," Proceeding of National Conference on Undergraduate Research (NCUR) 2011, Page 334-340, Ithaca College, March 31 – April 2, 2011.

Society memberships

American Physical Society (APS) Aug. 2009 - current

Abstract of the Dissertation

Surface modification is a versatile and effective route towards improving functional and structural characteristics of chemically synthesized nanomaterials. In the specific case of semiconducting nanoparticles (quantum dots) the photophysical properties are strongly tied to surface conditions. Therefore, a careful monitoring of photoluminescent (PL) behavior, both short and long term, is critical following alterations to their surface chemistry. We observe several noteworthy changes in the static and dynamic PL spectra of CdSe/ZnS core-shell quantum dots (QDs) when the as-grown native ligands are exchanged with two different mesogenic ligands – rod-like molecules attached to the particle by a flexible alkyl chain. These include reduced inter-dot energy transfer, stable recombination rates and steady emission color over more than an hour of continuous photo-excitation, all effects being more prominent in the sample with the longer attachment chain. Temperature dependence of PL and recombination rates reveals further differences. Thermally-activated PL recovery threshold is pushed to a higher temperature in the modified dots, while PL lifetime does not show the expected increase with decreasing temperature. Our results indicate that increased charge separation induced by the longer ligands is responsible for these effects, and this may be a route to fabricating quantum dot films for specific applications demanding long term emission color stability.

The design and development of multifunctional composite materials from artificial nano-constituents is one of the most compelling current research areas. This drive to improve over nature and produce ‘meta-materials’ has met with some success, but results have proven limited with regards to both the demonstration of synergistic functionalities and in the ability to manipulate the material properties post-fabrication and in situ. Here, magnetic nanoparticles (MNPs) and semiconducting QDs are co-assembled in a nematic liquid crystalline (LC) matrix, forming composite structures in which the emission intensity of the quantum dots is systematically and reversibly controlled with a small applied magnetic field (< 100 mT). This magnetic field-driven brightening, ranging between a two- to three-fold intensity increase, is a truly cooperative effect: the LC phase transition creates the co-assemblies, the clustering of the MNPs produces allows LC re-orientation at atypical low external field, and this re-arrangement produces compaction of the clusters, resulting in the detection of increased QD emission. These results demonstrate a synergistic, reversible, and an all-optical process to detect magnetic fields and additionally, as the clusters are self-assembled in a fluid medium, they offer the possibility for these sensors to be used in broad ranging fluid-based applications.

An important experimental realization resulted from the sensors. We found we could slightly modify the synthesis procedure by holding the temperature fixed approximately every 0.05 °C during the LC phase transition to generate ring-like NP structures. During the phase transition, the LC exists in a bi-phasic state which pushes the NPs to assemble in lines less than 1 µm. These rings still show potential to act as sensors, but are significantly smaller. However, to improve the sensors to be more sensitive, it became clear that we need to revise our model and mechanism behind the induced QD brightening. Namely, there is a scale mismatch between using optical microscopy to investigate, and the spatial reorganization happening on the nanoscale. By performing transmission electron microscopy (TEM), it was evident the MNPs have a tendency to remain dispersed in the LC, possibly due to stronger MNP aggregation and also stronger interactions to the sample surface, leading to the preference of “rings.” Furthermore, we investigated only MNPs in LC at the nano-scale when an external magnetic field is applied via Lorentz TEM and found that the LC matrix allows the MNPs to controllably rotate with the field, aligning their easy axis in such a way that generates a stronger net magnetization. It is this overall increase in magnetization that must be responsible for the spatial reorganization of the LC and subsequently the QDs, causing an increase in QDs per unit area and in turn the ensemble becomes brighter.

The main goal of this research combines both improving the stability of QDs and utilizing their fluorescent properties in magnetic field sensing devices. But, the mechanism for which this device works at the nanoscale is an important step toward making fluid-based processing a reality.

1 Introduction

1.1 Nanoparticles

Nanoparticles (NPs) are widely used in applications because their properties and tunability can be carefully selected to match desired functionality and these properties are not readily found in nature [1]. Semiconducting nanoparticles, or quantum dots (QDs), exhibit emission properties that result from quantum confinement and are used in optoelectronics [2] and biomedicine [3].

1.1.1 Semiconducting nanoparticles

Semiconducting nanoparticles, also known as quantum dots (QDs), are nanostructures which, when excited with light of a higher energy than their band gap, will emit photons whose wavelength depends on their band-gap [4]. As a QD absorbs light, an electron is excited into the conduction band and creates an electron-hole pair known as an exciton. After some amount of time (often, but not always, on the order of nanoseconds) the electron recombines and emits light with energy dependent on the band gap of the material. The bandgap is dependent on their diameter, a consequence of quantum confinement. This behavior differs from bulk material because the wavelength of an electron is close to the size of the nanostructure and thus crosses the bridge from classical mechanics to quantum mechanics. A simple approximation using the de Broglie wavelength can make this clear. A free particle with 3-degrees of freedom has energy:

$$E = \frac{3}{2} kT = \frac{1}{2} \frac{p^2}{m_e} \quad (1)$$

where k is the Boltzmann constant, T is temperature, p is momentum and m_e is the mass of an electron. Using room temperature, one can solve for momentum, and then use the de Broglie wavelength:

$$p = \frac{h}{\lambda} \quad (2)$$

and find a wavelength approximately of 6 nm. Any semiconducting nanostructure near this size may exhibit quantum confinement and have size-tunable light emission properties. This confinement causes unique properties not found in bulk and can be in either 1-, 2-, or 3-dimensions. The properties of the emitted light from a QD depends on the confinement length. To further investigate this phenomenon, one can solve the particle-in-a-box model to find energy:

$$E = \frac{\pi^2 \hbar^2}{2mL^2} \quad (3)$$

showing that the energy of the emitted photon is inversely proportional to the square of the length, L , or diameter of the particle. Furthermore, the QDs discussed in this dissertation are more similar to spheres than boxes, and solving the particle-in-a-sphere model yields a slightly modified confinement energy [4]:

$$E = \frac{\pi^2 \hbar^2}{8ma^2} \quad (4)$$

where a is the diameter of the sphere. Fig. 1 shows an example of colloidal QDs made from the same material being excited by near ultraviolet (UV) light with varying diameters. Starting with the smallest particles on the left, emitting green light, the QDs get larger to the right of the image. As the confinement decreases, so does the energy as seen in Equation (4), and thus the QD emission becomes more red, as wavelength is inversely proportional to energy.



Figure 1: Colloidal QDs

There are many materials and routes used to synthesize QDs. There are two major methods: top-down approaches commonly involving lithography and etching, and bottom-up approaches by chemically synthesizing QDs [5]. There are major advantages to either method. For top-down QDs, high lateral precision allows researchers to investigate the quantum confinement effect. For bottom-up QDs, these exciting nanostructures have been used extensively in opto-electronics [6,7], photovoltaic devices [8], biomedical applications [9], and many more areas of research. The focus of this dissertation is on chemically synthesized QDs. Through the processes to synthesize these nanoparticles (commonly microemulsion and sol-gel) [5], they have an inhomogeneous size distribution making the emission spectrum from an ensemble a Gaussian distribution. If the QDs were all the same size, the emission in solution, where there would be no significant interdot interactions, would be a dirac-delta function. With state of the art synthesis, this is currently not possible. Fig. 2 shows the spectra of drop-cast CdSe/ZnS core-shell QDs with a full width at half maximum (FWHM) of 30 nm. The absorption peak of these QDs is 620 nm and the emission peak is always red-shifted due to the Stokes shift.

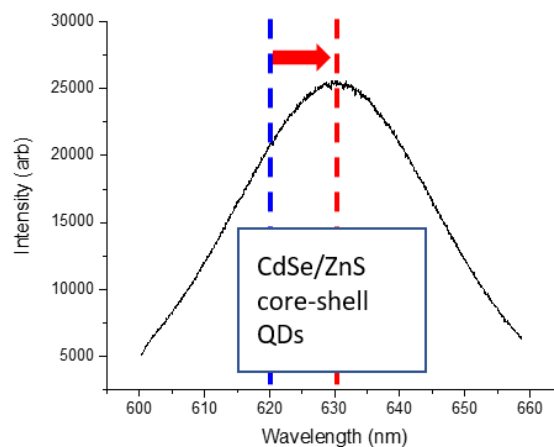


Figure 2: Spectra of colloidal QDs

In addition to the Stokes shift, ensembles of QDs with interparticle distances less than 10 nm exhibit a red-shift from energy transfer between smaller QDs (donors) to larger QDs (acceptors) via electric dipole-dipole coupling known as Forester Resonant Energy Transfer (FRET) [10]. The closer the interdot distance is, the more efficient the energy transfer (ET) and thus, the greater the red-shift. This can be very helpful when investigating the applications of QDs in this dissertation.

To further understand semi-conducting nanoparticles, a band diagram structure is helpful. QDs have a direct energy band gap between the valence band and the conduction band. As an excellent example from the Bawendi group, the QDs shown in Fig. 1 require approximately 2 eV to excite an electron into the conduction band [11]. QDs are commonly capped with an organic ligand overcoat to allow storage in solution, as well as protection from photo-oxidation. Fig. 3 shows the band diagram for CdSe core-only QDs (left) and CdSe/ZnS core-shell QDs (right). For core-only QDs, the electron wavefunction is largely confined to the core of the particle and only slightly extends into the surrounding organic matrix. The hole wavefunction is more centered to the core and doesn't extend into the surrounding matrix. For QDs with a shell of ZnS, the electron wavefunction tunnels into the shell and this delocalization lowers its confinement energy. For 2 nm CdSe/ZnS core-shell QDs, the barrier height is approximately 0.9 eV to tunnel into the ZnS shell and 4 eV to tunnel into the surrounding organic matrix, though this can vary based on synthesis.

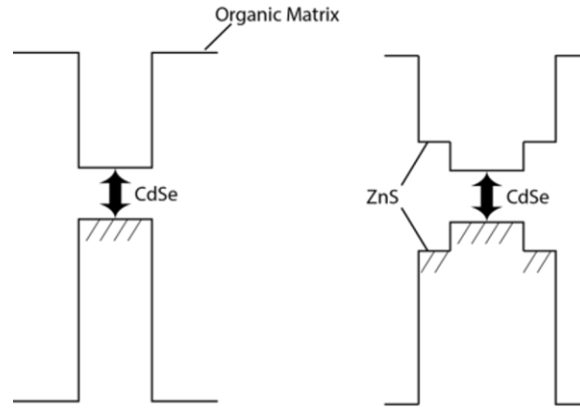


Figure 3: Band diagram of CdSe and CdSe/ZnS QDs [11]

Once an exciton is generated, the electron can either radiatively (emission) or non-radiatively recombine, e.g. generates a phonon. The average time that an exciton recombines in a QD is known as the recombination lifetime. In general, an ensemble of non-interacting QDs will have a single exponential decay (red line, Fig. 4). However, if there are additional processes, like energy transfer between QDs, the recombination lifetime will follow a bi-exponential decay (blue line, Fig. 4) and a sharp change can be seen in the decay at around 1 ns. The recombination rate, Γ , depends on a simple exponential decay function, with each addition process adding another exponential as follows:

$$\Gamma = e^{-t/\tau_1} + e^{-t/\tau_2} + \dots \quad (5)$$

For the QDs used in this dissertation, which have a CdSe core of approximately 6.2 nm, the lifetime in solution is approximately 13 ns and is single exponential at room temperature.

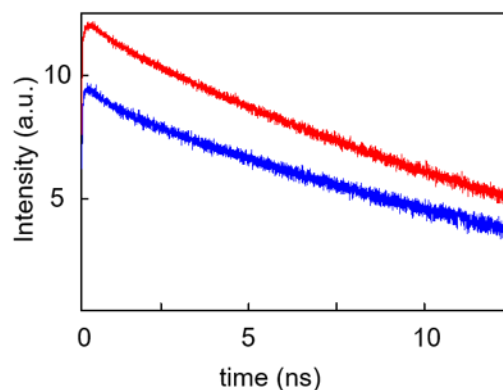


Figure 4: Recombination lifetime of CdSe/ZnS QDs

One such example of bi-exponential decay is caused by FRET. The lifetime of the smaller dots in the ensemble decreases overall as a result [12]. This is in contrast to the lifetime of QDs in solution, which involves no interdot interactions and thus solution lifetime is always the longest possible for a QD at a fixed temperature. The larger QDs in the ensemble exhibit a lifetime enhancement. As a result of FRET, the recombination lifetime of the QDs show a spectral dependence, where the smaller QDs in the ensemble have a shorter lifetime than in solution. Other sources of lifetime quenching can occur in QDs are in close proximity to metallic nanoparticles [13], due to charge separation by hole-accepting ligands [14], or photo-oxidation [15], to name a few.

While considerably more stable than conventional organic dyes which experience photo-bleaching and degrade rapidly, QDs do experience photo-induced instabilities in both vacuum and ambient conditions [15]. Typically, the emission of the QDs initially exhibit an enhancement of intensity when exposed to light in the presence of oxygen which is followed by a gradual darkening phase. The darkening phase is associated with photo-oxidation where non-radiative deep trap states are formed in the bandgap. Oxidation also causes a blue-shift of the spectrum as the formation of an oxide layer decreases the core diameter which increases the quantum confinement and the bandgap of the QD. QDs are most often synthesized so that they are capped with nonpolar organic molecules. This ligand overcoat, in addition to a QD shell, can prevent photo-oxidation to a certain extent. The ligand overcoat also allows for suspension in solution, further stalling photo-oxidation, as opposed to storing QDs dry. For increased functionality the ligands must be exchanged with a different molecule. Some examples are to improve the dispersion of QDs when embedding them into polar solvents, other materials, or improve charge separation to improve photovoltaic devices [14]. This can be achieved using a large variety of chemistries, including thiol and amine displacement.

1.1.2 Magnetic nanoparticles

Magnetism arises from the collective behavior of an ensemble of electrons or ions. Magnetic materials have several classifications. Diamagnetic materials, exhibited by most organic molecules, have a net magnetization that aligns against an applied magnetic field due to the tendency of electric charges to shield a body from an external magnetic field [16]. Paramagnetic materials become magnetized proportional to an externally applied magnetic field, but when the applied field is removed, the material does not retain a net magnetization.

The most common long-range ordered magnetic phase is ferromagnetism (FM). Ferromagnetic materials have a stronger net magnetization in response to an applied external field than paramagnetic materials, retain their magnetization if the external field is removed, and have a transition temperature

over which they become paramagnetic, called the Curie temperature. This transition temperature for bulk iron is very high, 1043 K, making magnetite (Fe_3O_4) an excellent material for examining magnetic effects at room temperature. The magnetic susceptibility of a material describes the influence of an external field on the magnetization of the material, and is given by the Curie-Weiss Law [17]:

$$\chi = \frac{C}{T - T_C}, \quad (6)$$

where C is dependent on the total angular momentum of the ions at each lattice point. An ion with no unpaired electrons, for example, would have a total angular momentum of zero and thus no magnetism.

An extremely important model used to understand the Curie temperature, phase transitions and spontaneous magnetization is the Heisenberg Model. The Hamiltonian for the Heisenberg model is [18]:

$$H = -J \sum_{i,j} \vec{S}_i \cdot \vec{S}_j, \quad (7)$$

which is a measure of the wave function overlap and type of coupling between ions. The energy is dependent on the separation and degree of alignment. J is the exchange integral and falls off exponentially as a function of distance. The exchange interaction is a purely quantum mechanical phenomenon that lies at the heart of long-range magnetic order. In the absence of an applied magnetic field, the spins will seek to minimize the free energy of the system. Anti-ferromagnetism is represented by an opposite sign on the exchange interaction as neighboring ions that anti-align will minimize the energy of the system, and is frequently a component for crystal lattices that exhibit interesting magnetic phases [19,20,21].

Domains in a bulk magnetic material are small regions that are all magnetized in the same direction [18]. Each domain is separated by a transition layer from the next one, where the magnetization is oriented in a different direction. If a NP is approximately the size of a magnetic domain in its bulk material then a collection of NPs can exhibit different magnetic effects than the corresponding bulk material.

Superparamagnetic ensembles of NPs can be aligned with an externally applied magnetic field and exhibit much larger magnetic susceptibility than paramagnets (10^3 to $10^5 \mu_B$). An ensemble of iron oxide nanoparticles may exhibit the superparamagnetic state below the blocking temperature [22].

Dense nanoparticle systems of magnetic NPs are likely to have slight variations of the inter-particle distances and anisotropic axis orientations. The strong-dipolar coupling between particles results in a positional disorder of the alignment of spins between neighboring nanoparticles similar to the positional disorder of glass, also known as super-spin glass [23-26]. The word 'super' refers to thousands of spins within a nanoparticle aligning with each other, thus acting like a single macroscopic spin.

1.2 Liquid crystalline materials

Liquid crystalline (LC) materials exhibit a phase between liquid and solid where the molecules display order over short range. Thermotropic liquid crystal materials change phase with temperature, as shown in Fig. 5A, an increase in temperature will transition a crystal into LC phase and then into the isotropic liquid phase. The LC molecules consist of a rigid core with a flexible tail and are often depicted as rod-like molecules. Though there are many mesophases that LC materials can exhibit, this thesis will focus on the nematic phase, N. In the N phase the molecules have short range orientational order in which the molecules tend to point in one direction, commonly referred to as the director axis, d. The LC molecule of interest in this thesis is the 4'-Pentyl-4-biphenyl-carbonitrile, or 5CB, which is shown in Fig. 5B. 5CB is a room temperature liquid crystal (20.5 °C) that transitions into the isotropic phase at 36 °C. Like many organic molecules, LC molecules are diamagnetic. Thus, ones with a rod-like shape will align parallel to an externally applied magnetic field above a critical field, H_C . This is called the Fréedericksz transition for a LC aligning to an external electric or magnetic field [27].

Due to their anisotropy, the LC phases are birefringent. Light interacting with the LC propagates at different speeds depending on the polarization of light and direction of the anisotropy. In addition to

being birefringent, the anisotropy of the LC molecules leads to the material having dielectric anisotropy. The material has one dielectric constant for electric fields parallel to the long axis, ϵ_{\parallel} , and a different one for electric fields perpendicular to the long axis, ϵ_{\perp} . From these we can define the dielectric anisotropy for a material, $\Delta\epsilon = \epsilon_{\parallel} - \epsilon_{\perp}$ where materials with positive $\Delta\epsilon$ will align with long axis in the direction of the applied electric field and those with negative $\Delta\epsilon$ will align with the long axis perpendicular to the applied field. A threshold exists below which an electric field can be applied to a bulk LC sample with no change. Above the threshold the molecules will reorient to align with the applied field. The reorientation of the director with applied field is called the Fréedericksz transition. This transition is used to create liquid crystal displays.

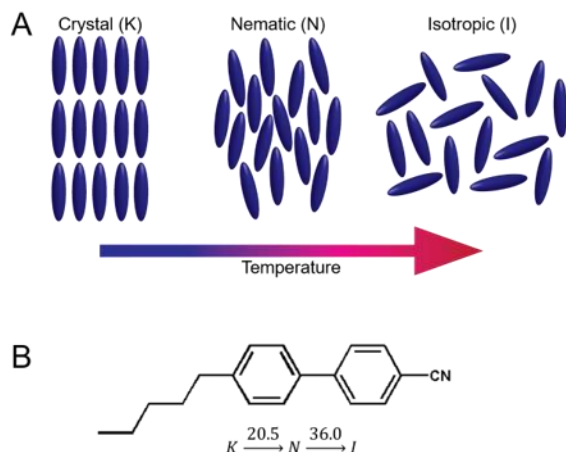


Figure 5: A) Schematic of phase transitions with increasing temperature. B) Liquid crystal molecule of interest, 5CB

1.3 Motivation

Nanoparticles offer unique opportunities to create devices that have behavior and functionality that cannot be found in nature due to their size tunable properties. The emission “color” of a QD can be tuned by changing the diameter, or adding a shell of a different material. The variety of devices available to QDs is extensive by using different compounds which varies the emission peak from UV (ZnO), to the visible spectrum (CdSe, CdS, perovskite), to near infrared (PbS, PbSe). ZnO QDs are relatively transparent to visible light and have been used in solar cells [28]. CdSe QDs have recombination lifetimes on the order of microseconds, and when doped with transition metals, they can be used for information processing, known as spintronics [29]. Because PbSe QDs have emission in the infrared, their emitted photons travel through tissue more readily than visible light and have been used for in vivo imaging [30]. It is important to note that QDs, like all NPs, are subject to photo-oxidation due to their large surface-to-volume ratio. In order to be truly cost effective in device applications, NPs have to be modified in some way (like a surface modification or ligand exchange) or even ordered in such a way that limits this process.

MNPs are an exciting subject for research on a fundamental scientific level and have been used in targeted drug delivery [31] and magnetic storage media [32]. Furthermore, the combination of QDs and MNPs into nanocomposite materials can provide even more functionality, taking advantage of both magnetic and fluorescence properties for multimodal imaging, in which magnetic resonance imaging and optical techniques are used [33].

The combination of LC materials and nanoparticles has been researched extensively. One avenue involves doping LC materials with NPs. Due to the extremely weak paramagnetism of LC molecules, the

external magnetic field required to align a LC cell is relatively high and prohibitive for effective devices that use magnetic fields and LC materials. Embedding MNPs in LC materials can change the Fréedericksz transition, lowering the threshold magnetic field required to change the LC orientational order [34, 35]. Another avenue is to use LC phase changes in a bottom-up approach to assemble NPs. There are top-down approaches in which metamaterials are made with nanoparticles and have been shown to change the index of refraction, but these approaches are not scalable [36, 37]. So, using LC materials create metamaterials using colloidal nanomaterials to do the same thing as these top-down approaches would be much more cost efficient. Unfortunately, this has not been realized yet, but the first steps into viable research in this field involves LC materials being used as a template to generate ordered arrays of NPs that can be used for composite materials with optical or magnetic functionality [38, 39]. Because the phase of LC materials can be modified *post situ*, one could potentially change an ordered array of nanoparticles in a LC matrix to exhibit different magnetic properties. One example of a possibility for magnetic functionality that is still yet to be researched is the ability to change the ensemble behavior of MNPs from paramagnetic to superparamagnetic and even ferromagnetic or super-spin glass. A device like this could combine data writing and data storage in one device, and when combined with QDs perhaps even information processing. Approaches like the ones in this dissertation could be the path to making fluid-based processing a reality.

Using LC materials as a template to direct the assembly of NPs has been studied extensively. Researchers have used LC materials to orient linear arrays of metallic nanorods which exhibit different luminescence behavior based on incident light polarization by trapping the nanorods in disclination lines in the LC [40]. There are many other types of LC phases used to assemble NPs with many different outcomes, using solvent polarity to control NPs in 1D [41] and spherical confinement of NPs with cholesteric LC [42]. The possibilities almost seem endless. The major challenge in this field is pushing these directed assembly processes from fundamental physics to regular use in devices.

MNPs in LC materials have been discussed and the combination of the two leads later in this thesis to magnetic field sensing technologies. To first understand the possible needs of this type of application, a discussion of the most common magnetic field sensors that do not use NPs is necessary. Magnetic field sensors are very useful, from thin film detectors used with computer disks to suspended magnets used for navigation. High- T_c (HTS) superconducting quantum interference devices (SQUID) rely on electromagnetic fields within a conductor or semiconductor in which a current is flowing through. The Lorentz force causes the movement of electrons in the material, most notably the Hall effect. HTS materials transition to superconductivity at a much higher temperature (40 – 80 K) and make the use of this type of device easier. SQUIDs are the most sensitive magnetic sensors, able to detect fields on the order of 10^{-12} T [43] and are used for measurements of the earth's magnetic field. SQUID-based systems do have drawbacks. These devices are expensive to make and require state-of-the-art signal processing to perform. The cooling systems necessary require further research to make SQUID-based systems more viable. As such, the application of these devices is still limited and so low temperature superconducting SQUID devices are much more common.

Giant magnetoresistance (GMR) technologies rely on the increase in resistivity of certain materials in the presence of an external magnetic field. GMR sensing devices were initially used in data storage. Fortunately, GMR sensing devices are much easier to use than HTS SQUIDs. These systems are non-linear, however, in their response to an external magnetic field due to hysteresis effects. Because of this, these devices are still largely under development. The sensitivity of these sensors is in the range of 10^{-3} T. There is GMR sensing work done in the biomedical field to detect double-stranded DNA using binding of MNPs to a sensor array [44]. While the exact sensitivity of the ability to detect magnetic fields is not measured, these systems can detect concentrations of DNA on the order of 10 nM.

Chapter 2 details the experimental methods used in this dissertation. Chapter 3 investigates the problem of photo-oxidation of QDs, which leads to a shrinking core diameter, and by equation 3 and 4 causes a blue-shift of the ensemble. In all devices where QDs are used, the QDs themselves are carefully chosen and tuned with an emission wavelength that matches the needs of the device, and when the peak emission wavelength changes, the device loses some viability. A ligand exchange is performed on the QDs a LC-like ligand which is larger than the typical organic ligand overcoat and this prevents the QDs from packing too closely. This, in turn, limits FRET and greatly increases the color stability of QD ensembles.

In chapter 4, we use a LC phase transition to assemble QDs and MNPs into 5 – 25 μm clusters which act as sensors that exhibit increased photoluminescence under the application of a small external magnetic field. These novel sensors do not require electrical leads, like Hall probes, for example. They are also extremely small, on the order of 10 μm thick. They are slightly reversible, and show potential for calibration. They exhibit synergistic behavior in which the MNPs magnetize, causing the LC material to reorient locally in such a way that causes the QDs to compact, and thus increase in brightness per unit area. In comparison to SQUID sensors and new GMR technologies, these sensors are significantly easier to produce, do not require state of the art signal processing nor extensive cooling systems, and remove the need for electrical leads.

In chapter 5, we slightly modify the synthesis procedure of the sensors in chapter 4 to generate ring-like nanoparticle (NP) structures in order to increase the versatility of these sensors. To do so effectively, it became clear that we need to revise our model and mechanism behind the induced QD brightening. Namely, there is a scale mismatch between using optical microscopy to investigate, and the spatial reorganization happening on the nanoscale. We first found on the nanoscale that MNPs, consisting of iron oxide have a tendency to remain dispersed in the LC, possibly due to stronger MNP aggregation and also stronger interactions to the sample surface. This leads to the potential to generate rings of NPs by modifying the cooling process from the previous chapter, but still exhibit induced brightening under the presence of an external magnetic field. Finally, we investigate only MNPs in LC at the nano-scale when an external magnetic field is applied via Lorentz TEM. In doing so, the LC matrix allows the MNPs to controllably rotate with the field, aligning their easy axis in such a way that generates a stronger net magnetization. It is this overall increase in magnetization that must be responsible for the spatial reorganization of the LC and subsequently the QDs, causing an increase in QDs per unit area and in turn the ensemble becomes brighter.

The sensors outlined in chapter 4 and 5 of this thesis are much different. While not as sensitive as the SQUID devices, their sensitivity approaches that of some GMR devices [43]. However, these sensors offer huge advantages. Due to the bottom-up approach using the LC material to assemble the NPs, the cost to generate these sensors is reduced significantly. Also, unlike SQUID and GMR devices, there is no need to detect the field by passing a current through them. This also removes the need for complicated computing equipment and noise reducing software. Finally, these sensors are completely optical, providing a huge advantage over HTS SQUID and GMR devices.

Chapter 2

Magneto-optical Kerr Effect Microscopy

2.1 Magneto-optical Kerr effect

The magneto-optical Kerr effect (MOKE) was first discovered in 1875 [2-01]. Light is an electromagnetic-wave and will interact with a magnetic material. The reflection of polarized light by a magnetic material can cause rotation of polarization, induced ellipticity, and a change in intensity [2-02]. Linearly polarized light will hit a non-magnetic sample and will retain the same polarization. The focus of this dissertation is on linearly polarized light reflecting from a magnetic sample and causing a change in the linear polarization angle, known as the Kerr angle, θ_K .

There are three major types of MOKE microscopy: polar, longitudinal, and transversal geometries. These depend on the plane of incidence and the applied magnetization to a sample. In the following chapters, only polar and longitudinal MOKE are used. For polar MOKE, the magnetic field is perpendicular to the magnetization direction and parallel to the plane of incidence. This can be done with normal incidence in which the microscope objective is perpendicular to the sample. For longitudinal MOKE, the magnetization is parallel to the sample surface and perpendicular to the plane of incidence. Unlike polar MOKE, this cannot be done in normal incidence for magnetic samples, however, the birefringence of a LC sample can still be measured.

Any sample with optical anisotropy will produce a Kerr effect. LC materials, for example, which are birefringent, will result in a change in the polarization of reflected light. In magnetic samples, like iron-oxide magnetic nanoparticles, θ_K is proportional to magnetization. θ_K is a small rotation, on the order of microradians in the samples measured in this dissertation. The complex Kerr angle is:

$$\theta_K \approx \tan \theta_K = \frac{2}{1-\varepsilon} [-(k_- - k_+) + i(n_- - n_+)] \quad (1)$$

Here, k_+ and k_- (n_+ and n_-) is the absorption (birefringence) for left and right circularly polarized light respectively, $(k_- - k_+)$ is circular dichroism and $(n_- - n_+)$ is circular birefringence. In order to effectively measure the Kerr angle, a photoelastic modulator (PEM) is required because of the extremely small signal. The PEM causes large swings in the index of refraction, and when combined with a lock-in amplifier, allows for accurate measurement of the small signal that is the Kerr angle. Ultimately, the complex Kerr angle, becomes [2-03]:

$$Re[\theta_K] = \frac{1}{4J_2(\beta)} \frac{I_{2\omega PEM}}{I_0} \quad (2)$$

$$Im[\theta_K] = \frac{1}{4J_3(\beta)} \frac{I_{3\omega PEM}}{I_0} \quad (3)$$

In these equations, β is the setting on the PEM (usually π), $I_{2\omega}$ and $I_{3\omega}$ are the readings from the lock-in amplifier for the 2nd and 3rd harmonic, and I_0 is the reflected intensity. By comparing these to equation (1), equation (2) relates to the circular dichroism and equation (3) relates the imaginary component, circular birefringence.

2.2 Optical setup

Fig. 1 shows the optical setup used to measure the photoluminescence of QD emission and the MOKE signal of both MNPs and the LC material. By switching the flip mirrors either up or down, one can go back and forth between scanning for QD emission or the MOKE signal. The lock-in amplifiers are connected to the PEM and the photodiode.

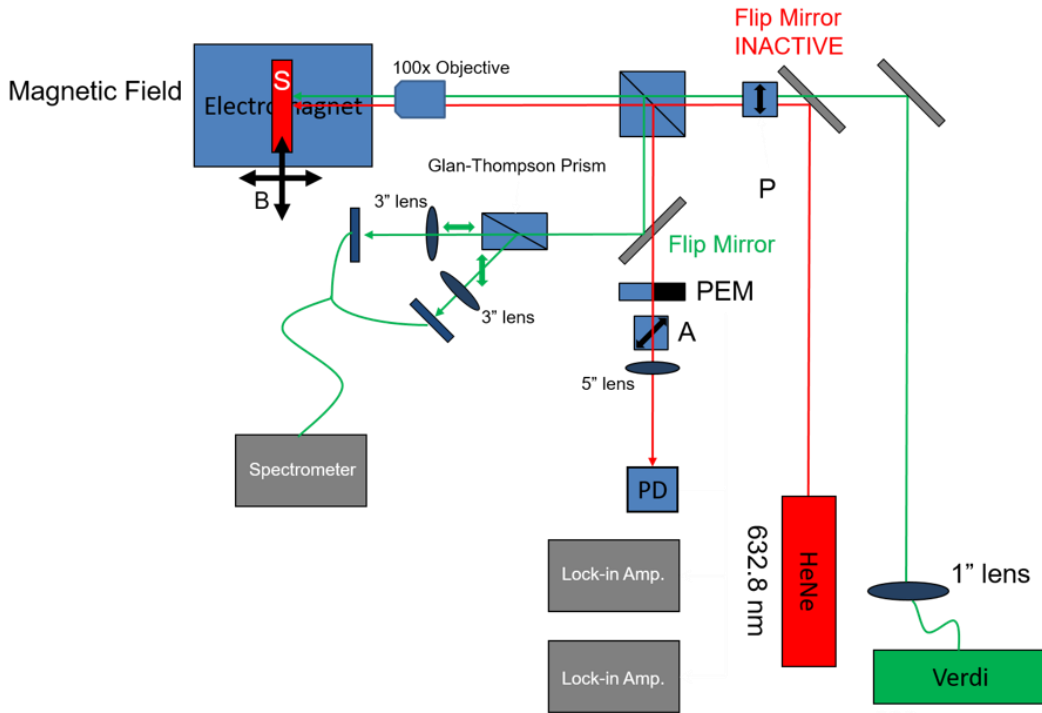


Figure 1: Combined setup for MOKE and photoluminescence

2.3 Experimental data

Two examples of MOKE measurements used in Chapter 4 are shown in Fig. 2. For MNPs shown in Fig. 2A, when a magnetic field is applied, the Kerr angle rotates according to a typical paramagnetic curve. If the applied field were to increase past 2.5 kG, the Kerr angle would eventually level off. In Fig. 2B, a sample of LC material doped with MNPs is displayed. Because the signal from LC birefringence dominates the signal from a small amount of MNPs (less than 0.1 wt%), the data trend is largely reflective of the thresholding behavior of the Fréedericksz transition. One can approximate the threshold field by fitting two lines to the first half (0-3 kG) and the second half (3-6 kG) and recording where the two lines intersect as the threshold field.

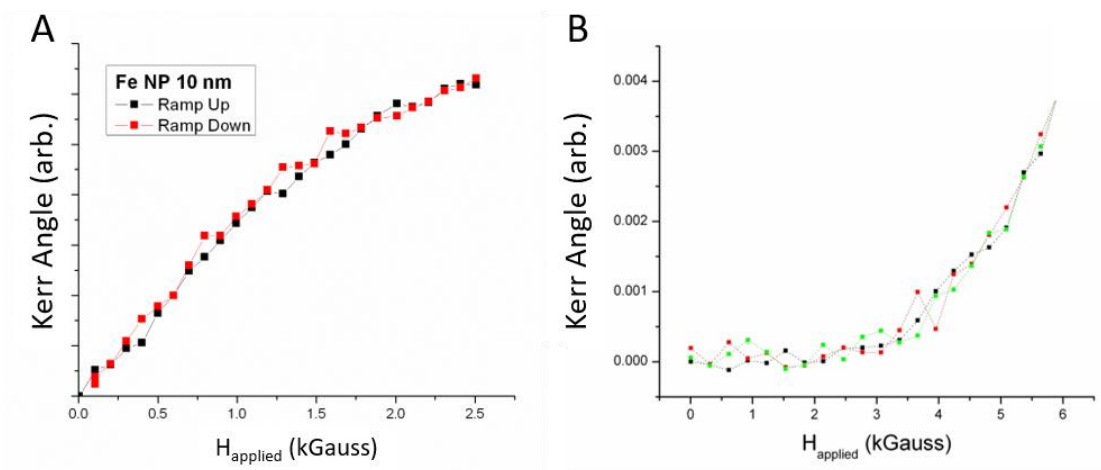


Figure 2: MOKE measurement of MNPs. MOKE measurement of LC material doped with MNPs.

3 Effect of mesogenic ligands on short and long-term spectral dynamics and stability of core-shell CdSe/ZnS quantum dots

3.1 Introduction

Surface modification of chemically synthesized semiconducting quantum dots (QDs) not only plays a critical role in determining the optical and electronic properties of the nanoparticles, but also affects the chemical stability and sample longevity [1-3]. As-synthesized QDs are coated with surface ligands primarily to prevent aggregation of the dots and to keep them suspended in the native solvent [4]. It is most common for these ligand molecules to be hydrophobic, as typical end-product solvents are non-polar. However, post-synthesis ligand exchange is often carried out for a variety of end goals. Common examples include allowing suspension of QDs in water or water-based solvents for biocompatible products [5,6], enhancing photo-stability and prolonging shelf-life of QDs used in photo-detectors [3] and hastening charge transport by exchanging longer surface ligands for short molecules for photovoltaic applications [7]. A specific niche where QD surface chemistry plays a central role is in the development of hybrid materials, such as liquid crystal- or polymer-QD composites, where miscibility of the dots in the host medium is key to uniform dispersion [8] or to selective spatial organization [9]. Commonly used ligand molecules, such as octadecylamine (ODA), oleic acid (OA), or trioctylphosphine oxide (TOPO), result in QDs aggregating in the host, particularly when dispersed at the high concentrations needed for device development. The presence of a NP within a LC material disrupts the order of the LC, as a higher elastic energy cost is required for the LC molecule to arrange themselves around the NP. ODA, OA, and TOPO extend radially outward around the NP and the surrounding LC molecules align with the ligand overcoat creating a hedgehog defect. In these cases, custom ligands structurally similar to the host molecules are required, and for liquid crystalline media these are known as mesogenic (liquid crystal-like) ligands (MLs). By changing the ligand overcoat to a ML, the ligands themselves can align with the LC phase and alleviate the some of the extra energy cost required to embed NPs within. Surface modification with various MLs has been attempted with the specific aim of improving the dispersions of QDs (as well as other types of nanoparticles) in liquid crystal (LC) media [10]. All ligand exchange processes alter the surface of the QDs and therefore lead to changes in spectral absorption, quantum yield [11], recombination lifetimes [12] and other related optical and electronic properties, not only in the short term post-modification, but in the long term as well. In the case of surface modification using MLs, while basic spectral properties such as quantum yield are usually documented following ligand exchange, the focus is largely on studying the dispersion of the QDs within the host phase with the goal of understanding guest-host interactions, rather than long-term QD behavior. It is important to characterize and understand these long-term changes, to allow rational design for improved functional and structural stability.

We present a study of the effects of surface modification in 6.2 nm diameter CdSe/ZnS core-shell QDs (with 5% size inhomogeneity in a typical ensemble). When the original octadecylamine (ODA) ligands are substituted with mesogenic ligands, we find several spectral changes that result from our surface modification, especially with respect to how the QD ensembles behave under continuous and prolonged photo-excitation. The most striking result is that the emission color is stabilized considerably, in effect arresting photo-oxidation completely.

3.2 Experimental Details

The two MLs used in this work are shown in Fig. 1. They consist of a rigid aromatic core, designed to couple to the QD surface via a flexible amine-terminated alkyl chain linkage (3 or 6 carbons long) highlighted in dashed boxes. ODA simply consists of a linear 18 C-atom long alkyl-terminated chain. The ligand exchange process follows the precipitation-redispersion scheme outlined in detail in [10]. Without ligands, NPs will aggregate and fuse together. Our QDs already have a ligand on the surface. An amine

ligand wouldn't displace the existing ligand. So, the ligand must be stripped off using acetone or some other solvent. QDs are then re-dispersed in a solvent with the new ligand. ODA, the amine is attracted to the surface. Other ligand exchange processes replace one ligand with another that has a higher affinity for the NP surface. Some types of ligands are chemisorbed – chemically attached like a thiol to a metal NP in a covalent bond. To remove the sulfur bond would remove atoms from the NP. These ligands are physisorbed – an electrostatic attraction, or dative bond, not covalent.

For optical measurements, drop-cast films of QDs with ODA (QD-ODA) and with mesogenic ligands (QD-MLA/B) are prepared by allowing slow drying of QDs deposited on clean substrates, following [13]. For static spectral measurements, a Coherent CUBE laser excites the samples at 409 nm with excitation power of 28 μ W and the data is collected by an Acton 300i spectrometer dispersed onto a thermo-electrically cooled CCD (resolution \sim 0.18 nm). For time-correlated measurements, an ultrafast tunable Ti:Sapphire laser is used as the optical excitation source, frequency-doubled to 409 nm with an excitation power of 30 μ W. The detector is a single photon avalanche diode coupled to a time-correlated single photon counting (TCSPC) system (PicoHarp 300) with an instrument response function of 12 ps, positioned after a monochromator. All room temperature measurements are conducted in ambient conditions using a Nikon 100X objective with a diffraction limited resolution of \sim 500 nm. For temperature dependent studies the samples are mounted in an Advanced Research System cryo-free system capable of temperature control in the range 300-10 K. Transmission electron microscopy (TEM) images are obtained with a JEOL-2010 TEM equipped with a LaB₆ filament and operated at 200 kV in the Imaging and Microscopy Facility, UC Merced. TEM samples are prepared by placing 0.2 μ L of solution diluted to 10% of original concentration on a TEM copper grid with carbon film, wicking excess solvent, and placed in a vacuum oven for \sim 4 hours to remove residual solvent. Small angle X-ray scattering (SAXS) measurements are carried out at the Stanford Synchrotron Radiation Lightsource, beamline 4-2 at 11 keV. SAXS transmission experiments were carried out on thin film samples dropcast in toluene and deposited on Kapton[®] film using a 1 mm \times 300 μ m beam profile. Data was collected using a CCD detector and analyzed using custom SasTool software available at the beamline.

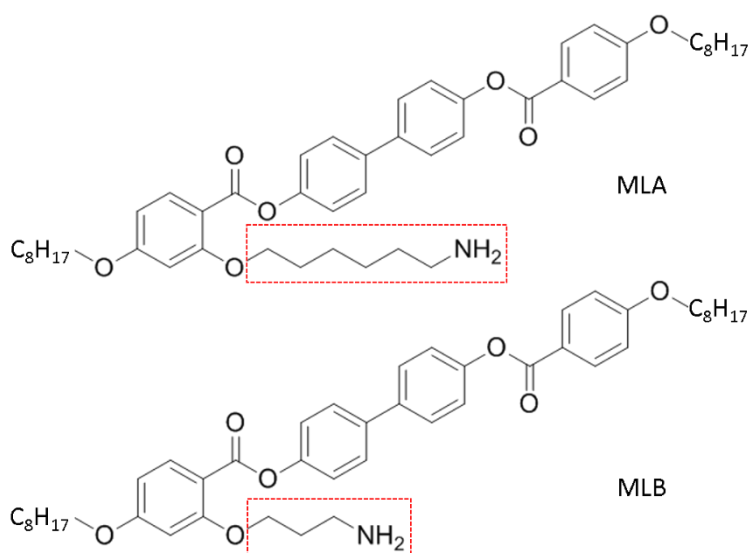


Figure 1 Chemical structure of the two mesogenic ligands. The dashed enclosures highlight the difference in the linker chain between the two.

3.3 Results and Discussion

QDs with ODA, when densely packed, tend to be highly close-packed as the flexible ODA ligands interdigitate to some extent. This is a typical result from dropcast NPs – during evaporation of the solvent the NPs arrange close to each other to minimize surface tension of the solvent. The NPs are not in a perfect hexagonally close-packed. There is natural disorder in the resulting ensemble of NPs because of the evaporation of the solvent and the ligands themselves. However, their arrangement is similar. A TEM of a sample prepared this way is shown in Fig. 2A. By contrast, the MLs are much more rigid due to the aromatic cores and there is some evidence that the ligands associate with these cores arranged laterally, stabilizing NP packing with an increased particle separation compared to ODA [14]. TEM images of QD-ODA and QD-MLA films are shown in Figs. 2(A) and 2(B), respectively. The distributions of nearest neighbor (NN) distances between the dots averaged over a $1 \mu\text{m}^2$ region in these images are shown in Fig. 2(C), calculated using ImageJ software [15]. This calculation is done with a nearest-neighbor distance plug-in by Yuxiong Mao. Every particle in the image is identified by an outline, and then the distance to the closest neighboring particle (surface-to-surface) is recorded in a table, one value for each particle. The data is normalized to the mode of the distributions as a ± 2 nm error in the image analysis renders the actual separation values inaccurate. However, comparison of the plots reveals a tighter NN separation within the QD-MLA film despite the overall packing fraction being smaller compared to QD-ODA. The characteristic inter-dot separation in the films is derived from the SAXS data shown in Fig. 2(D). The positions of the scattering peaks are determined by subtracting a baseline from the raw data, producing inter-dot separations of 9.4 nm for QD-ODA, and 10.4 nm for QD-MLA. The QD-MLB films were expected to have a particle spacing intermediate to these values, given the shorter linker length (Fig 1), but in these SAXS measurements we observed an average dot separation similar to QD-MLA.

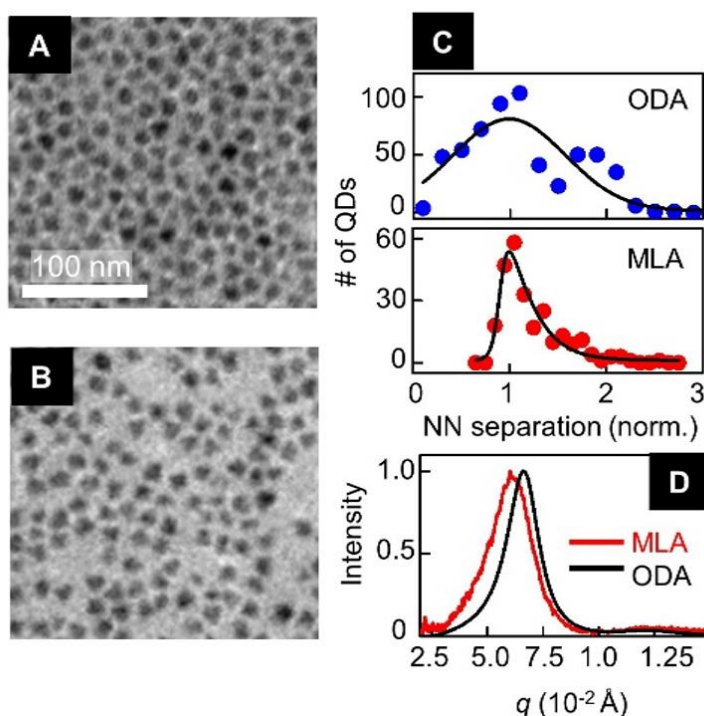


Figure 2 (A, B) TEM images of QD-ODA and QD-MLA samples, respectively. (C) Nearest neighbor separation of QDs for the two samples, normalized to the modes of their distributions. (D) SAXS data collected for dropcast films of QD-MLA and QD-ODA on kapton.

The observed increase in inter-dot spacing due to the mesogenic ligands is expected to reduce energy transfer (ET) in QD-MLA/B films, as ET in QDs is dipole-mediated, scaling as $1/r^6$ where r is the inter-dot separation [16]. This decreased ET can be seen in Fig. 3(A), which shows spatially-resolved maps of PL intensity and the corresponding peak wavelength of a $50 \mu\text{m}^2$ area of a QD-MLA film (solution emission centered on 636 nm). The intensity map (left) is largely homogenous with the exception of two bright spots at the top, corresponding to regions of high QD density. Typically in such crowded spots ET is very efficient and the emission is shifted to longer wavelengths (red shift). The map of the peak wavelength (right) for the same region varies between 643-644 nm (red-shift of 7-8 nm), including the spots of high density. In QD-ODA films similar measurements routinely show spectral red-shifts of 10-12 nm.

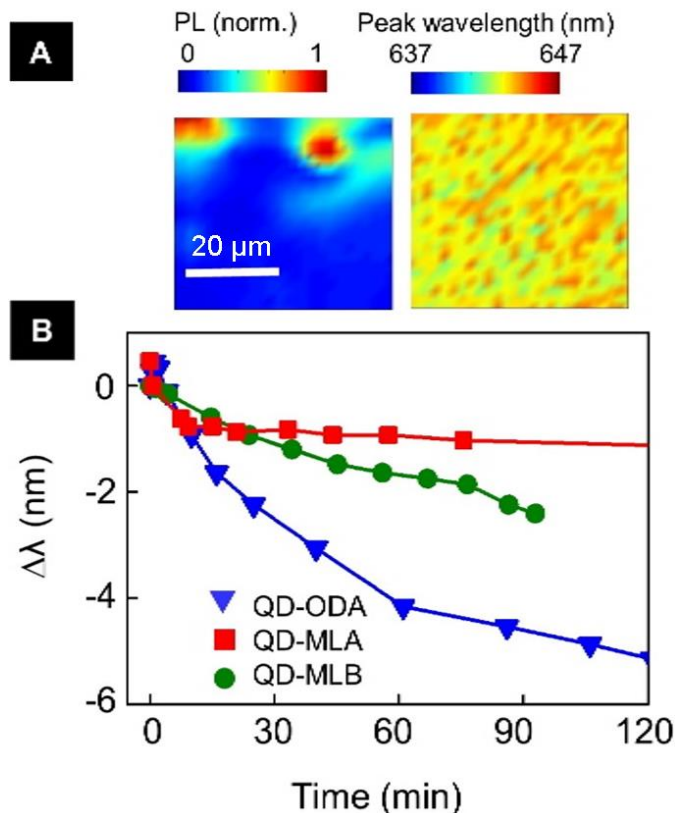


Figure 3 (A) Spatially-resolved maps of PL intensity (left) and peak wavelength (right) of the same area of a QD-MLA film. (B) Peak spectral shift as function of photo-excitation time.

In our earlier work we established that ET increases photo-darkening rates in larger dots within an ensemble, even in a nominally single color collection. Therefore, reducing in the QD-MLA films should be advantageous to the QD ensemble in terms of photo-stability. To investigate this, we monitor the PL of QD films over a period of 120 min under continuous excitation, and plot the peak emission shift, $\Delta\lambda$, in Fig. 3(B). $\Delta\lambda$ is measured from the peak emission at the start of photo-excitation (designated '0' on the time axis). QD-ODA blue shifts rapidly by 4 nm in the first 60 min and then slowly by another 2 nm in the next 60 min. QD-MLB performs better, exhibiting approximately a 3 nm shift over the entire 100 min period. QD-MLA is noticeably better than both, shifting only by 1 nm in the first 10 min and then stabilizing completely beyond that. Spectral blue shift is indicative of oxidation of the QD core, which reduces the core diameter and results in increased quantum confinement. Lack of an observed significant blue shift is therefore a very encouraging sign. We analyze this further and de-convolute the inhomogeneously

broadened spectrum into two subsets by fitting it as a cumulative of two Gaussian distribution. These represent the smaller dots (donors) and the larger dots (acceptors) that participate in intra-ensemble ET. We show one example in Fig. 4(A), noting that while in reality the ensemble spectrum is a superposition of more than two distributions, this simple model allows us insight into how the spectral weight redistributes with photo-excitation. In Fig. 4(B) we track the peak positions of each of these subsets with time for QD-ODA (top) and QD-MLA (bottom) films. In both types of QD films each subset blue shifts linearly with time, although with varying rates. QD-ODA film has stronger intra-ensemble ET than QD-MLA, confirmed by the longer wavelength peak positions of the subsets at the start of photo-excitation. As a result, the acceptors blue-shift faster than the donors, as has been observed in close-packed QD films [13]. By comparison QD-MLA shows that the blue-shift rate for the acceptors and the donor spectral emission is far smaller over the entire time.

The effect of reduced ET and arrested photo-oxidation in QD-MLA/B extends to dynamic PL aspects as well. Figs. 4(C-E) plot spectrally-resolved PL recombination lifetimes of the three types of QD films. The spectral positions where the time-resolved data are taken are indicated in Fig. 4(A) with symbols (downward triangle, circles, and upward triangles) commensurate with those used in the plots. The time-resolved traces are mono-exponential, a sign of weak inter-dot interactions. We extract the lifetime τ from these traces with $I(t) = I_0 e^{-t/\tau}$ and comparing the three, note that lifetimes τ increase with emission wavelength, a consequence of ET. At the start, the difference between the lifetimes of the blue to red emitting dots is greater in the QD-ODA films than the others, as also expected from the reduced ET in QD-MLA/B samples. The actual lifetimes seem to scale inversely with the ligand length, from longest in ODA to shortest in MLA functionalized dots. The trend exhibited by the lifetimes changing with photo excitation time is also strikingly different: the QD-ODA shows a steep increase at the longer wavelengths in the first 60 min, followed by a decrease. The lifetimes at other wavelengths show little (at peak of emission) to no changes (at blue end). This trend is characteristic of close-packed QD films with typical ligands and at even longer times, the curves have been seen to actually converge. Incidentally, the first 60 min is also when the spectrum undergoes the rapid blue-shift shown Fig. 3(B) and the increasing lifetime of the larger dots is a direct consequence of this. As some of the acceptor dots oxidize, they also go dark and do not contribute to the ensemble PL. The QD-MLA and QD-MLB films both show a 2-5 ns increase over the entire time window, while the difference between lifetimes at different wavelengths is unchanged. This long time stability of recombination lifetimes is highly unusual in dense QD films and is a testament to the lack of photo-induced damage in these dots.

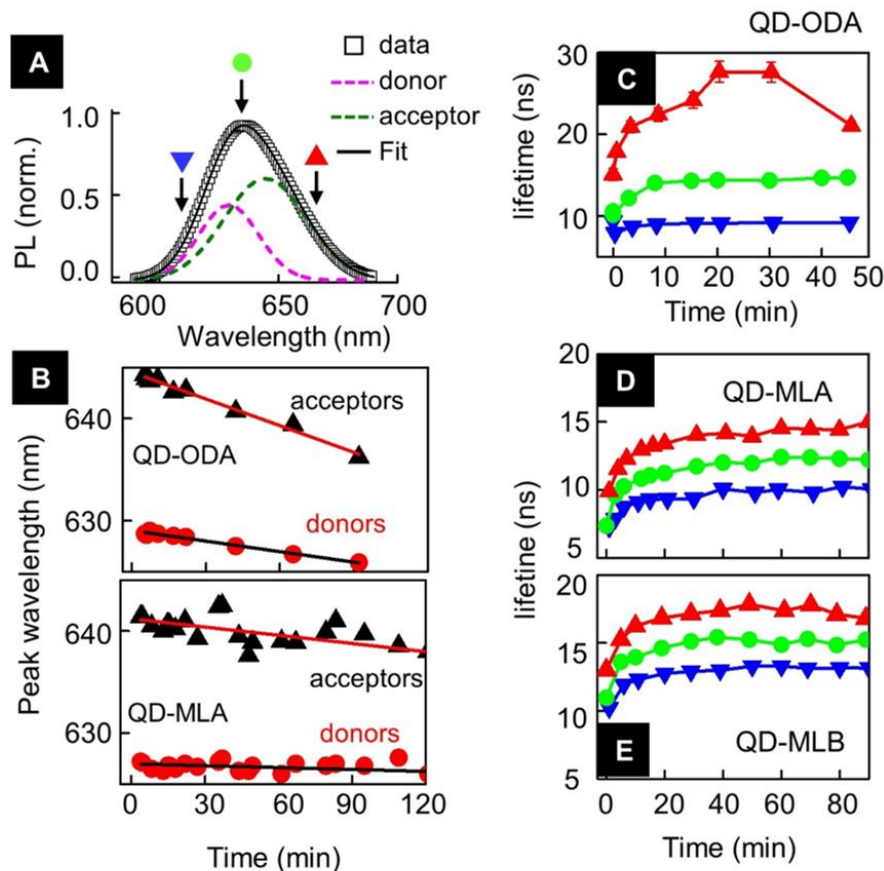


Figure 4 (A) Representative QD emission spectrum fitted with two Gaussians, designated the donor and acceptor subsets. The symbols indicate spectral positions where data in C-E are taken. (B) Peak wavelength of the two subsets shifting with photo excitation duration for QD-ODA and QD-MLA samples. (C-E) Spectrally-resolved PL recombination lifetimes for QD-ODA, QD-MLA and QD-MLB samples tracked with excitation time. Symbols explained in A.

Summarizing our results so far, the mesogenic ligands appear advantageous in several respects, including emission color and lifetime stability, with the slightly longer MLA performing the best. The one detrimental aspect is the slightly reduced PL lifetimes compared to QD-ODA dots. For further insight into this we look at temperature dependent static and dynamic PL. QD properties are strongly modulated by thermal changes, and these studies highlight any subtle changes in surface properties and energetics resulting from ligand exchange. In Fig. 5(A) we plot the integrated PL intensity with temperature T in the range of 300-20 K for QD-ODA and QD-MLA films. Both types of QDs show similar trends, where the intensity is quenched at low T followed by a recovery (anti-quenching) and saturation at higher T . The recovery threshold is almost 100 K higher in the QD-MLA film. Anti-quenching is symptomatic of suppression of non-radiative recombination channels brought about by thermally induced carrier activation [17-19]. Prior studies have demonstrated that with increasing ligand length, the PL recovery is pushed to higher T , a result of the surface states moving farther from the core of the QDs and not due to worsened surface quality [20]. Spectrally-integrated time-resolved PL data in Figs. 5(B) and 5(C) in the same temperature range are all single-exponential, confirming lack of significant non-radiative recombination. The inset in Fig. 5(B) plots the lifetimes obtained from fits to the time-resolved traces with

temperature. Neither sample shows any significant changes with T , but QD-ODA lifetime appears to begin a sharp rise around 100 K, while QD-MLA lifetime remains fairly constant. PL recombination in QDs above 20 K is governed by the thermal equilibration between the allowed (“bright”) and forbidden (“dark”) states that are separated by a few meV. Following analysis in [21] we plot the recombination rate Γ_L (inverse of lifetime) vs T in Fig. 5(C) inset. The data is fit to:

$$\Gamma_L = \frac{\Gamma_A + \Gamma_F}{2} - \frac{\Gamma_A - \Gamma_F}{2} \tanh\left(\frac{\Delta E}{2 k_B T}\right)$$

where Γ_A and Γ_F are the recombination rates of the allowed and forbidden states and ΔE is the energy splitting between the two. For QD-ODA we obtain $\Delta E = 2.9$ meV and $\Gamma_A = 0.087$ ns⁻¹; QD-MLA fit returns marginally different values of $\Delta E = 2.6$ meV and $\Gamma_A = 0.095$ ns⁻¹. The mesogenic ligands have aromatic benzene rings where the π electrons serve as efficient conduits for charge transfer when stacked closely, by capturing the photogenerated holes. Functionalizing QDs with similar “hole accepting” ligands has been reported to cause PL quenching and faster recombination [22]. We observe a reduced lifetime for both mesogenic ligands in Fig. 4 and an increased Γ_L in Fig. 5(B). The unchanging lifetime at $T < 100$ K for QD-MLA in Fig. 5(A) is likely also a consequence of exciton dissociation via charge transfer. The decreased energy splitting between the bright and dark states is an additional indicator of reduced electron-hole overlap. Neither of these changes are very great, implying the surface modification does not affect the dynamic properties of the dots to any significant extent. The room temperature spectrally-integrated lifetime of the QD films τ_F in the inset of Fig. 5(A) can give us an estimate of the ET efficiency η , using $\eta = 1 - \tau_F/\tau_S$ where τ_S is the recombination lifetime of isolated dots in solution. We calculate an efficiency of 20% for QD-ODA and 9% for QD-MLA, which is in agreement with our previous observation that ET is reduced following functionalization with the mesogenic ligands.

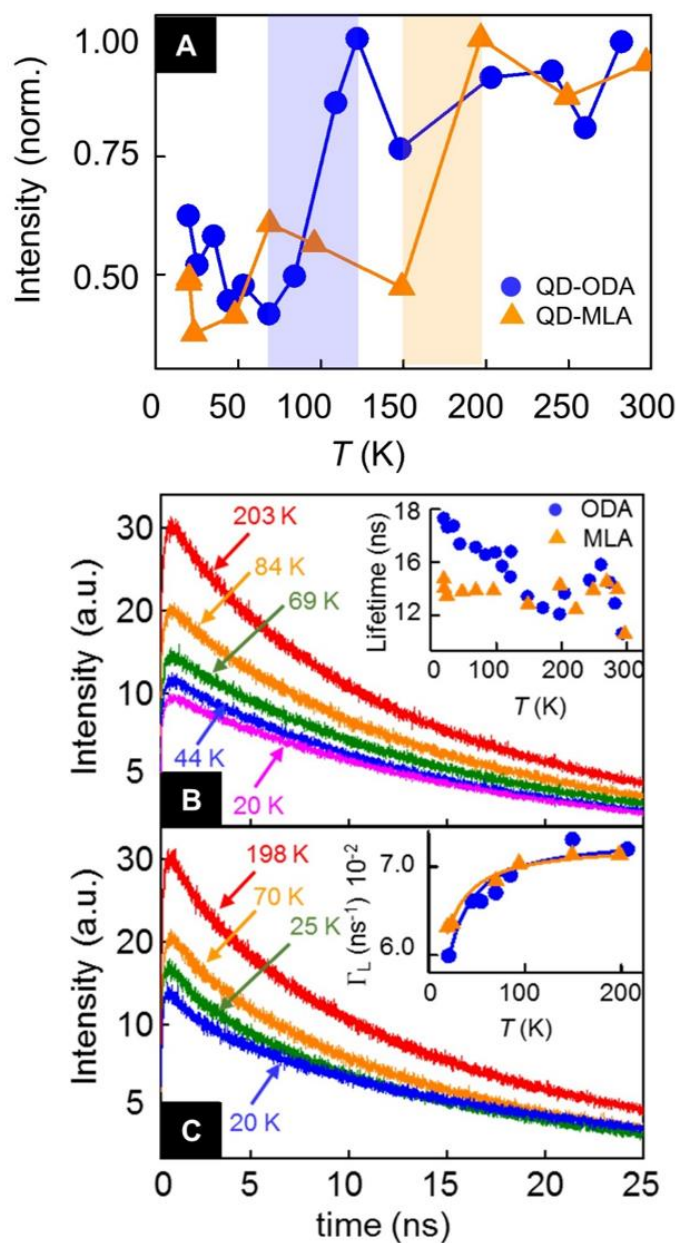


Figure 5 (A) Integrated PL intensity for both types of QDs varying with T . Shaded regions indicate the PL recovery threshold. Time-resolved PL as functions of temperature T for (B) QD-ODA and (C) QD-MLA samples. (B, inset) Lifetimes from single exponential fits for the two samples. (C, inset) Recombination rates derived from the samples. Lines are fits described in the text.

3.4 Conclusion

The use of these liquid crystalline molecules to functionalize nanoparticles was motivated by the drive to develop hybrid materials with added functionalities. In the case of QDs, this modification allows better dispersion in liquid crystal hosts [10], templated assembly into three-dimensional architectures [14] and possibly novel photonics applications [23]. We have demonstrated that these surface modifications are

sustainable where long-term QD properties are concerned and in some aspects, lead to improved optical performance in close-packed films, such as stabilization of both emission wavelength and recombination dynamics. There is considerable effort invested in developing photo-stable QDs, particularly for photovoltaic applications where long-term exposure to high photon flux is unavoidable. The most successful of these are the 'giant' QDs, so named because of a thick shell that removes surface states from proximity to the core [24]. Achieving stability via surface modification is a more general route that could lead to improved performance by all QDs, allowing for more widespread usages.

4 Magnetic field induced brightening in liquid crystal synergized magnetic and semiconducting nanoparticle composite assemblies

4.1 Introduction

A relatively new development in materials research is the use of NPs as ‘building blocks’ to design superlattices that would form meta-materials with functionalities significantly modified from those of individual constituents [1]. The most common approaches include traditional bottom-up assembly of NPs, which has successfully created two- and three-dimensional superlattices with up to three different types of particles and the synthesis of hybrid core-shell composite nanostructures [2-4]. These avenues have yielded structurally well-ordered arrays extending over microns, but the functional aspect has been less compelling. Most of the superlattices formed this way tend to simply exhibit the combined properties of the constituent NPs, instead of exhibiting a novel functionality arising from synergistic inter-particle interactions. An alternative route is to use soft materials (polymers, liquid crystals, biomolecules, etc.) as templates for NP assembly [5-8], since long-range crystalline order is not required to observe synergistic functionalities. A soft host would remove rigid constraints in the way the individual components can be combined and make novel architectures possible, such as non-planar structures. Additionally, it would allow in situ modulation of the NP assembly via external controls, such as temperature, mechanical strain and electromagnetic fields, which could lead to greater versatility in functionality or even to the emergence of entirely novel behaviour.

In this study, we co-assemble semiconducting quantum dots (QDs) and magnetic nanoparticles (MNPs) directed by the nematic phase of a liquid crystal (LC) [9], and reversibly control the QD emission via a small applied magnetic field. Our choice of LC as the host material is motivated by several factors. The LC phases exhibited by a material can be fine-tuned via careful control of molecular structure. LC materials are optically anisotropic and therefore birefringent, which means they can be manipulated to produce macroscopic domains with a defined optical axis. In several LC phases, molecular orientation can be further controlled by external electric and magnetic fields. They are, therefore, ideal materials to form a switchable matrix for dynamic NP assembly [10,11]. The multifunctional combination of semiconducting and magnetic materials is a very attractive one with great potential for application in two widely different fields. The first is in the computing/information processing industry, where a magnetic semiconductor could simultaneously handle both data storage and processing. Research efforts in this area continue to make progress [12], but are less focused on colloidal nanomaterials. The second field is biological/biomedical sciences [13,14], where chemically synthesized semiconducting and magnetic NPs are widely used. The high quantum yield of fluorescence and relative optical stability of QDs has made them popular for cellular tagging, imaging, and sensing. In the case of MNPs, their directional response to magnetic field gradients is exploited for cell separation and drug delivery, among other applications. Recently, there has been some preliminary progress in using formulations combining fluorescence and magnetic properties for multimodal imaging [15,16]. Our study has significant advantages over these current findings, as it demonstrates a strategy for the self-assembly of densely-packed NP clusters that can be modulated via their electro-optically active host to exhibit synergistic behaviour that is considerably modified from that of the individual particles.

4.2 Results and Discussion

4.2.1 Assembly and structural characterization of nano-composites

We disperse 6 nm CdSe/ZnS core-shell QDs (ligand: octadecylamine) and 10 nm Fe₃O₄ MNPs (ligand: oleic acid) in a nematic LC, 4'-pentyl-4-biphenylcarbonitrile (commonly known as 5CB). The QDs emission spectrum is centered at 630 nm in solution with a FWHM of ~ 30 nm. The MNPs are optically inactive and paramagnetic at room temperature. 5CB is nematic at room temperature and is used to both facilitate the assembly and stabilize the NP clusters. Figure 1a shows a series of fluorescence microscopy images demonstrating the temperature evolution of the composite material on cooling, and the subsequent co-assembly of the clusters. When the LC is in the isotropic phase, the NPs form a uniformly mixed, stable dispersion. Cooling at a rate of 0.1°C/min to a temperature below the clearing point (34.4°C) results in the NPs gradually being excluded into less ordered regions of the LC to minimize the elastic deformation energy cost to the system [9]. The final picture is shown in Figure 1a at 34.1°C where each bright point is a cluster of NPs. Average cluster size is 10 – 20 μm and the average separation 50 – 100 μm , but these values are dependent on the cooling rate and initial QD concentration, with faster rates yielding smaller clusters. Prior studies on LC mediated QD assembly suggested that within each cluster the particles are arranged in irregular aggregates, but the inter-dot separation is uniform throughout [9]. The transmission electron microscopy (TEM) image of a QD cluster in Figure 1b appears to confirm this, where a loose fractal-like NP assembly can be observed. Small angle x-ray scattering (SAXS) results reveal further details about the co-assembly process. Transmission scattering from clusters in the LC phase yields broad diffraction peaks indicative of the average QD-QD separation in the cluster. In Figure 1c we plot the scattering vector, q , for the observed peaks for a series of samples with varying proportions of QDs and MNPs. For QD-rich and MNP-rich samples, we observe single peaks in q that correspond to 8.9 nm and 12.5 nm NP separations, respectively. These numbers are consistent with expected nearest neighbour distances between close-packed QDs and close-packed MNPs, after accounting for the shell and surface ligand interdigitation. In the range of QD:MNP ratios of 1-1:2, both of these length scales are present, but there are no indications of a third diffraction peak, or any peak broadening, suggestive of QD-MNP close-packing. These observations lead us to conclude that the different NPs form segregated domains within the clusters. The schematics in Figure 1c combine the above TEM and SAXS results to depict a possible arrangement within the co-assembled clusters, and we follow up with the functional characterization using photoluminescence (PL) and magneto-optical Kerr effect (MOKE).

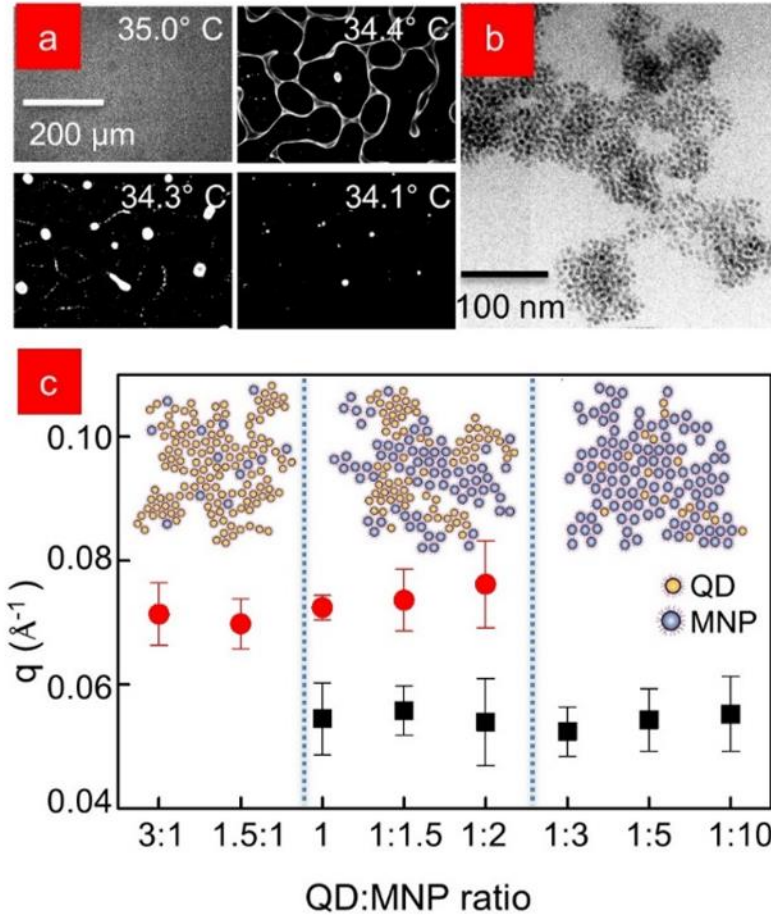


Figure 1. (a) 10 nm magnetic Fe₃O₄ nanoparticles (MNPs) and 6 nm CdSe/ZnS core-shell quantum dots (QDs) dispersed in isotropic liquid crystal (LC), 5CB. As 5CB is cooled through the I – N phase transition, co-assemblies of MNP-QD form in disordered LC regions (b) TEM image of a QD-only assembly formed by the same method, surveyed through the host LC. (c) SAXS results of a series of MNP-QD samples in 5CB, showing the observed diffraction peaks of the scattering vector q varying with the relative ratios of the two NPs. Dashed lines indicate the NP concentration region that allows the best chances of co-assemblies forming. (insets) Schematics of co-assembled clusters showing the segregated domains of QDs and MNPs.

4.2.2 Synergistic emission enhancement in nano-composites

The PL of a QD ensemble divulges information about almost all fundamental properties, including its size distribution and absence or presence of inter-dot interactions. MNPs are optically inactive and we need to use a different imaging technique. MOKE [17] is the rotation upon reflection of the incident linear polarization of an excitation laser beam in response to any optical anisotropy in a sample. We use the polar MOKE configuration, with the magnetic field B applied out-of-plane and the linearly polarized excitation laser in near normal incidence (Figure 2a). The angle of this rotation is called the Kerr angle, θ_K . In the case of magnetic materials where the magnetization M imparts anisotropy in permittivity ϵ , $\theta_K \propto M$, and for our collection of paramagnetic NPs, the magnetization follows a linear relation $M = \chi\mu B$ (χ : susceptibility, μ : permeability). This linear relation is verified for a drop-cast film of MNPs and shown in Figure 2b (black triangles), which also shows Kerr rotation from a sample of nematic LC (red circles) for

the same range of B . Although not magnetic, the structural anisotropy of LC molecules makes them birefringent, and this makes them responsive to MOKE measurements. At low applied B , this shows up as a constant offset. However, at higher B , analogous to their response to external electric fields, the LC molecules re-orient and the resultant Kerr rotation is plotted in the inset to Figure 2c. The black arrow defines the critical threshold field B_c for re-orientation. For an LC material like 5CB the critical field B_c is high (~ 0.5 T) due to its small χ , but theory and experiments have established that on doping with MNPs, this threshold decreases [18,19]. In Figure 2c we plot B_c for 5CB doped with MNPs over a range of concentration Φ , and find that it satisfies the canonical relation $B_c \propto \Phi^{-1/2}$ [20,21]. Since we restrict our applied B to < 100 mT and MNP concentration less than 0.1% wt., the θ_K contribution from LC molecules near our NP clusters should be magnetic field-independent, allowing us to de-convolute it easily from the θ_K of MNPs.

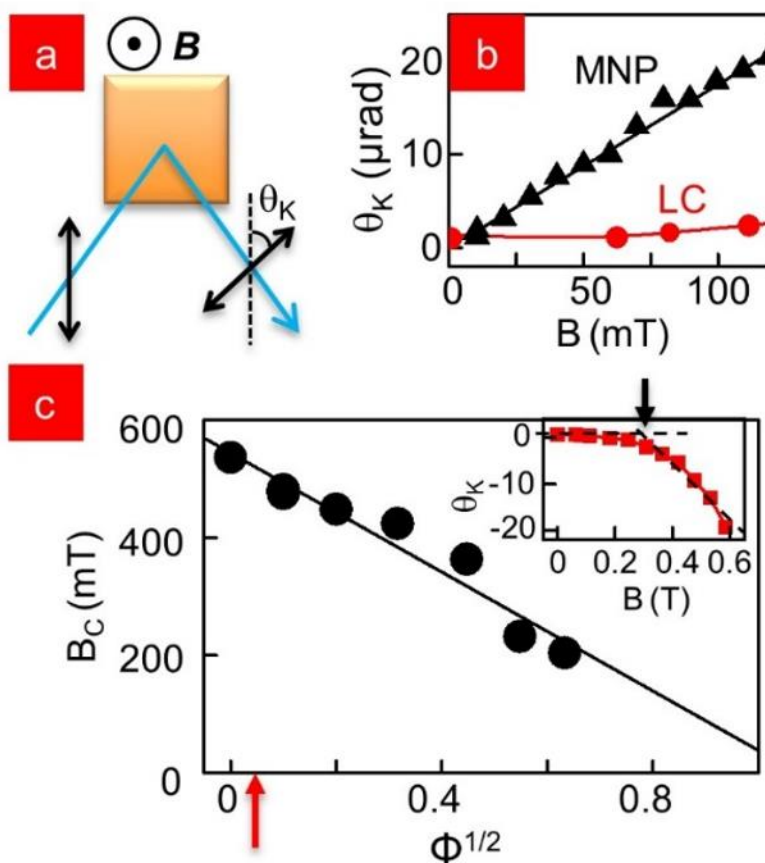


Figure 2 (a) Schematic of the technique of MOKE (b) Kerr angle θ_K for MNPs and LC molecules at low B (c) (inset) MOKE measurement showing LC switching with B . Arrow denotes the critical switching field B_c . (main) B_c as a function of MNP concentration Φ . Red arrow shows the MNP concentration used specifically for this study.

Figures 3a and 3c are spatially-resolved maps of the PL emission intensity and θ_K of a collection of two neighboring clusters at $B = 0$ in a homeotropically aligned LC matrix. PL signal marks the location of QDs in the clusters in Figure 3a and at positions that correlate to the centers of the PL spots, Figure 3b shows localized high θ_K values, indicating the possibility of MNPs in those regions. The remaining area has $\theta_K \neq 0$, in spite of the induced homeotropic alignment of the LC, where the molecules should be pointing out-

of-plane and not contribute to birefringence for light incident along the same direction. In fact, this is typical as the LC molecules are disordered around the co-assembled clusters and have an approximate radial arrangement in that region. The PL and MOKE scans are repeated over the same spatial region at $B = 17.2$ mT in Figures 3c and 3d. The PL intensity (Figure 3c) increases between two- to three-fold in the clusters compared to the $B = 0$ mT data and θ_K shows a two-fold increase in Figure 3d. The spatial consistency between PL and MOKE images confirms for the first time that the QDs and MNPs do co-assemble in the clusters. This result is further supported by the SAXS results, validating our schematic in Figure 1c. The MOKE map also shows areas surrounding the clusters where θ_K decreases on the application of B . This implies a birefringence change caused by reorientation of the disordered LC molecules in the direction of B and appears to contradict our data in Figure 2c, which postulates that at the concentration of MNPs used (red arrow), $B_c \approx 500$ mT. But it can be explained by recalling that those results and all prior observations are based on the study of LC samples with relatively uniformly dispersed MNPs. In our case, in spite of very low total Φ , the cluster-assembly process produces localized regions of high concentration of MNPs. The total magnetic moment of these regions possibly generates a high enough field over a few microns at small external fields to bring about spatial re-orientation of the disordered, and therefore, weakly anchored, LC molecules immediately surrounding the MNP clusters.

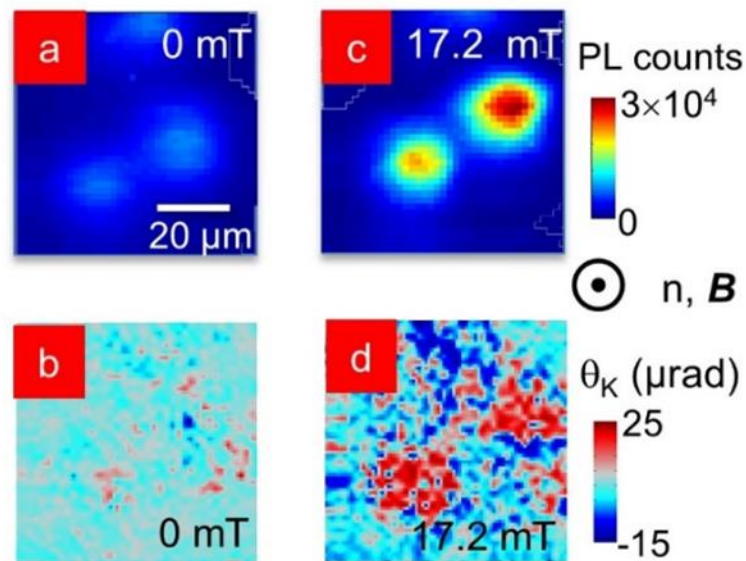


Figure 3 Spatially-resolved PL intensity scan of MNP-QD co-assembly in 5CB at (a) 0 and (c) 17.2 mT. Corresponding spatially-resolved MOKE images of the same assemblies at (b) 0 and (d) 17.2 mT. Scale bar in (a) refers to all images.

4.2.3 Systematic and reversible optical magnetic sensing

We track the PL enhancement observed in Figure 3c with B systematically and plot the PL intensity integrated over the entire scanned region of a cluster in Figure 4a. The cluster is shown in the inset to the main figure. We observe an initial linear rise that approaches saturation around 80 mT. As a reference, M of the MNP clusters is linear in this regime (Figure 2b) and do not approach saturation until $B > 700$ mT. Ensembles of QDs often exhibit spontaneous photo-induced brightening under constant illumination, and we rule out a similar effect by (a) ensuring the excitation power is always extremely low ($< 18 \mu\text{W}$), (b) performing PL scans under identical conditions in control samples with only QDs in LC, and (c) reversing

the direction of magnetic field change. We verify the reversibility of this effect in Figure 4b by taking PL scans at 0, 41.2 mT and 82.5 mT (marked by open circles in Figure 4a) while ramping the field up, and then again at 41.2 mT and 0 while ramping down. For each iteration of B we allow an equilibration time of 10 min. We note that the PL enhancement is reversible, although slightly hysteretic.

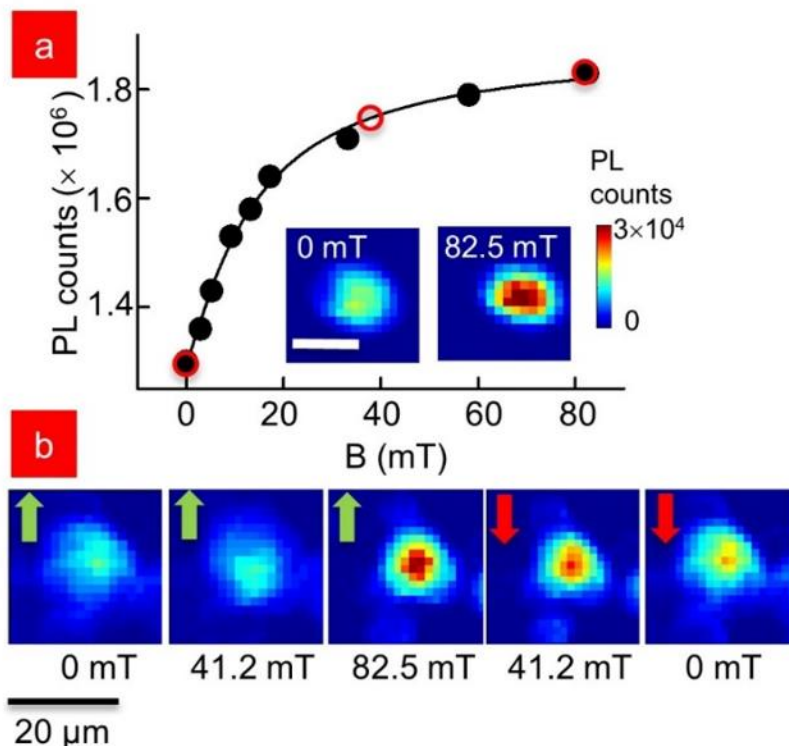


Figure 4 (a) (inset) PL intensity map of QD-MNP cluster at 0 and 82.5 mT (main) Spatially-integrated PL intensity of the cluster plotted as a function of applied magnetic field (b) PL intensity maps at magnetic field value indicated by red circles in (a) while ramping up (green arrows, $0 \rightarrow 82.5$ mT) and down (red arrows, $82.5 \text{ mT} \rightarrow 0$).

This PL enhancement is very intriguing, as there is no straightforward explanation for two- to three-fold QD PL enhancement at such low B . We ruled out photo-induced QD brightening, and the only other instance of CdSe QDs exhibiting increased emission intensity with magnetic field occurs at very high B (~ 10 T) [22]. For more information, we plot the peak emission wavelength λ_p of the QDs in this cluster in Figure 5a. In an ensemble of densely packed QDs, the smaller dots transfer energy to the larger ones, causing a resultant red-shift of the emission spectrum. This mechanism, known as FRET (Forster resonant energy transfer) is well understood [23], and it allows λ_p to be used as a ruler to measure inter-dot separation, which in turn reflects the strength of inter-dot coupling. In solution, when the QDs are isolated with no inter-dot interactions, $\lambda_p = 630$ nm, but in Figure 5a ($B = 0$) the emission is centered between 635 – 638 nm, suggesting the QDs are close-packed as evidenced in the SAXS measurement of Figure 1c. Comparative λ_p map at $B = 82.5$ mT shows no significant increase in median λ_p distribution across the cluster, which suggests the average inter-dot spatial separation remains unchanged and the increased magnetic field does not alter any fundamental inter-particle coupling. SAXS results confirm this result as well. Since it is therefore unlikely that the emission from the individual QDs changes with the application

of the field, the net increase in the integrated intensity seen in Figure 4a over the field of view must come from a corresponding increase in the number of QDs within the imaging volume. A visual inspection of the λ_p maps does highlight an apparent change in the cluster size, and in Figure 5b we plot line profiles from the corresponding PL intensity maps (Figure 4a, inset), and the data confirm a symmetric spatial compression with increasing B . We estimate the percent increase in QDs in the imaging volume from this by evaluating $n=100d/((100-d))$ where d is the measured decrease of cluster diameter with B . In Figure 5c we plot n as a function of B concurrently with the relative change in PL intensity, f , and find that they compare very favourably. By the maximum applied B , f shows a total change of almost 40% in integrated PL emission while the spatial compaction predicts an increase in QD density of 36%, off by a mere four percent. But while these estimates suggest the observed effect is related to a compaction of the clusters, the question that arises is how are the clusters shrinking without decreasing the average inter-dot separation?

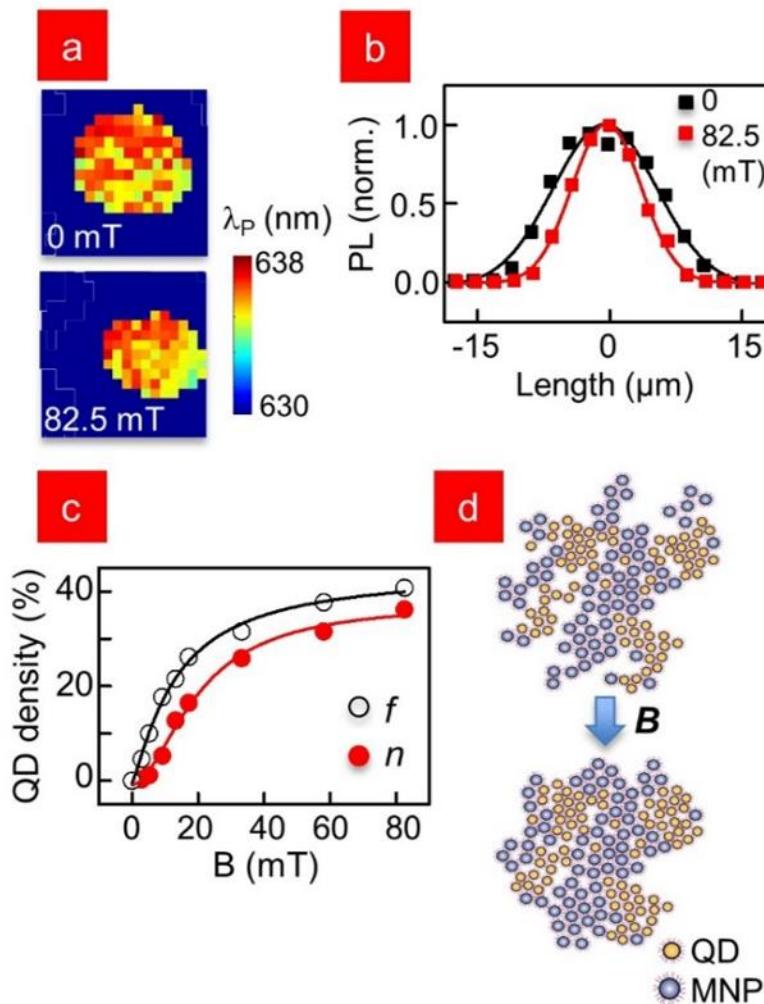


Figure 5 (a) Spatially-resolved map of peak wavelength λ_p for the cluster in Fig. 4a (b) Profiles of the PL intensity of cluster in (b) for 0 (black) and 82.5 mT (red) (c) QD density increase estimated from PL intensity, f and spatial compaction measurements, n (d) Schematic showing the compaction of the MNP-QD clusters with magnetic field.

We schematically depict a possible mechanism in Figure 5d. Prior to the application of B the internal structure of the cluster is an irregular and inter-connected network of aggregates with constant inter-particle spacing as typically seen for diffusion limited particle aggregation. Inter-particle separation is defined by partial interdigitation of surface ligands and the interstitial regions are occupied by the LC molecules. Initial LC orientation in and around the cluster should be approximately radial with local disorder, and this is detected in the θ_k map in Figure 3b. The locally induced magnetic fields from the collective dipole moments of the MNPs within the cluster cause the surrounding LC molecules and those inside the interstitial spaces to locally align along the externally applied B . In a feedback-like process this alignment induces compaction of the aggregates accompanied by expulsion of the voids, thus minimizing elastic deformation to the locally more aligned LC medium. The removal of the external B and subsequent thermal relaxation of the system, results in the LC molecules slowly returning to their original orientations, thus the clusters are released from their tighter packing arrangement and can open back out.

4.3 Conclusions

This spatial re-alignment and re-organization of the LC molecules in and around the clusters that leads to QD PL enhancement is a result of the cooperative behavior between the QDs, the MNPs and the LC material they are suspended in. The LC defect-templating creates the clusters from a dispersed isotropic state, the clustering of the MNPs produces the localized high fields that cause LC re-orientation at low external B , and this re-arrangement produces compaction of the clusters, resulting in the detection of increased QD emission. Given the very low external field required to produce the large two- to three-fold brightening we observe, and that the intensity change follows a well-defined function of the applied field and can be used to calibrate it, these clusters could be used as low magnetic field optical sensors. Our results demonstrate a truly synergistic, reversible, and an all-optical process to detect magnetic fields that is completely non-invasive and low loss, bypassing any need for electrical connections. As the nanoparticle clusters are self-assembled in a fluid medium and remain suspended in it, with future modifications, it would be possible for our sensors to be used in broad ranging fluid-based applications.

4.4 Materials and methods

Sample preparation: Nematic liquid crystal 4'-pentyl-4-biphenylcarbonitrile (5CB, Sigma Aldrich) is mixed with 2 mg/ml octadecylamine coated CdSe/ZnS core-shell QDs (NN Labs) and 5 mg/ml oleic acid coated iron-oxide MNPs (NN Labs) in toluene to a concentration of 0.02 to 0.05 wt% at QD:MNP ratios ranging between 2:1 – 1:10. The QD-MNP-LC mixture is bath sonicated at 50 °C so that the LC is in the isotropic phase for 6-18 hours to obtain even NP dispersion, verified by optical microscopy. To do so, you simply take a very small amount (1-2 μ L) of the LC and check on a heating stage when the transition temperature occurs. If it is far from the transition for pure 5CB, there is likely too much solvent remaining or too high a wt% of NPs. The dispersion of QDs should be checked in the same way to ensure they are sufficiently dispersed within the LC. For optical imaging, clean glass slides are dip coated with aqueous hexadecyltrimethylammonium bromide (CTAB) solution (1% by wt.) for one hour and dried under nitrogen to produce a homeotropic LC alignment layer. For a planar LC alignment layer, glass slides are spin-coated with poly-(methyl-methacrylate) (PMMA) and dried under nitrogen and then rubbed with a velvet cloth with uniform strokes. Samples are sealed with a similarly coated glass cover slip. To form the clusters, samples are cooled below the LC clearing temperature at 0.1°C/min using a Linkham LTS350 hot-stage.

Spectroscopy and imaging: For QD PL measurements, a 532 nm continuous wave (cw) excitation laser is focused on the sample through a 100X Nikon objective to produce a diffraction-limited spot diameter of approximately 600 nm. Samples are mounted on a motorized high-resolution scanning stage, and spectra recorded with an Acton 300i Spectrometer which disperses the signal onto a thermo-electrically cooled CCD camera. For MNP imaging, magneto-optical Kerr effect (MOKE) measurements are taken with

a cw He-Ne laser (632 nm). A photo-elastic modulator is used to modulate the signal at 50 kHz, and the Kerr rotation resolved using a standard lock-in amplifier technique with a resolution of 0.2 μ rad [24]. For best MOKE results, there should be no other laser light incident on the photo detector, and this can be handled by a collimating pair in the collection path with an iris placed at the focal point between the two lenses. High-resolution PL spectroscopy and MOKE measurements are performed in the same setup with two collection paths, which allows simultaneous fluorescence and magnetic imaging of the NP co-assemblies.

Small angle X-ray Scattering (SAXS): Measurements were carried out on Beamline 4-2 at Stanford Synchrotron Radiation Lightsource. Samples are prepared as for microscopy, and dispensed into 1.5mm quartz x-ray capillaries for unaligned (powder) small angle scattering and exposed to an 11KeV x-ray beam for 0.5s in a custom-built mount with variable magnetic field. Diffraction patterns are recorded on a CCD detector, then plotted as integrated intensity as a function of q , the scattering vector using analysis software available at the beamline.

5 Generating ring-like structures of nanoparticles and nano-scale investigation of magnetic nanoparticle rotation leading to enhanced local magnetization

5.1 Introduction

This chapter seeks to improve upon the magnetic sensors from the previous chapter. Due to the size mismatch between optical microscopy and the nanoparticles (NPs) in the structures themselves, we sought to perform electron microscopy to investigate NP structure, spatial reorganization and behavior on the nanoscale. In doing so, we hope to better understand the morphology and reaction of these sensors to an external magnetic field, which may lead to increased sensitivity of the sensors. Additionally, the fundamental knowledge provided may give insights into the potential of fluid-based processing with devices like the one in chapter 4. Also discussed in this chapter is a change to the experimental procedure which leads to the formation of NP rings within the host liquid crystal (LC). These structures are smaller and exhibit a similar induced brightening, and with further modifications may lead to smaller, more sensitive sensors.

Magnetic nanoparticles (MNPs) properties stem from confinement as well as surface effects, and an ensemble can have an increased magnetic susceptibility compared to bulk allowing for easier manipulation in applications that require a magnetic field [1]. The combination of magnetic and fluorescent nanomaterials is an ideal combination for drug delivery in which medicine can be moved magnetically in a magnetic field gradient [2], tracked fluorescently while improving MRI contrast [3], and have an increased uptake in infected cells [4]. Controlling the nanostructure outcome of a NP assembly process is an extremely important area of research.

A bottom-up approach to constructing new materials involves embedding NPs in soft matter, such as LC materials, and this avenue is an important research field because LC responds to electric and magnetic fields which can in turn act as an optical switching device [5] or utilize the NPs in microscale devices for sensing applications [6]. Using LC materials to assemble NPs is often aimed solely at generating novel structures [7]. Doping LC materials with MNPs has been researched extensively as a means to reduce the threshold field required to change the alignment of the LC material, known as the Fréedericksz transition [8]. While assembly of nanoparticles in liquid crystal materials has been done extensively, this paper highlights the only application where an external magnetic field is used to modify the properties of a sample post fabrication and *in situ* [9]. Additionally, this research focuses on colloidal nanomaterials in fluid-based mediums and understanding the processes governing spatial reorganization of such a sample.

In this study, we use a LC thermotropic phase transition in which we keep the temperature constant during crucial points to assemble quantum dots (QDs) and magnetic nanoparticles (MNPs) into ring-like micro-scale clusters that can be manipulated *in situ* by application of a small magnetic field (<250 mT). The micro-scale clusters act as a magnetic field sensor that does not require electrical connections similar to our previous work which involved compact clusters that were not ring-like in structure [9]. However, to fully improve the synthesis technique and maintain precise control *in situ*, our previous investigation of these sensors on the microscale was inadequate. We need to examine the nanoscale behavior. To do so, we generate assemblies in LC, and then perform elemental analysis via STEM, in addition to Lorentz TEM which allows us to apply a magnetic field. These important steps lead to understanding the nano-assemblies synergistic functionality.

5.2 Experimental

5.2.1 Nanoparticle co-assembly preparation

For the following procedures, we use two types of nanoparticles (NPs) and a nematic liquid crystal (LC). The magnetic nanoparticles (MNPs) are Fe₃O₄ NPs (NN-labs) with a 10 nm diameter and oleic acid (OA) ligand overcoat stored in toluene solution. The quantum dots (QDs) are CdSe/ZnS core-shell NPs (NN-labs)

with a 6.2 nm core diameter and an octadecylamine (ODA) ligand overcoat stored in toluene. The LC material in use is 4'-pentyl-4-biphenylcarbonitrile (5CB, Sigma Aldrich).

For TEM samples of QDs and MNPs without LC, 0.2 μL of stock solution (2 mg mL^{-1}) diluted 1:10 is deposited directly onto Cu TEM grids with a carbon film (400 mesh, Ted Pella Inc) and then placed in a vacuum oven at 40 $^{\circ}\text{C}$, -25 mmHg, for \sim 2 hours to evaporate residual solvent.

To form co-assemblies of MNPs and QDs in LC, we mix the MNPs with 5CB at 0.04 %wt and sonicate at 40 $^{\circ}\text{C}$ for 3-6 hours. Then CdSe/ZnS core-shell QDs (NN-labs) with a 6.2 nm core diameter and an octadecylamine (ODA) ligand overcoat (toluene solution) are added to the mixture at 0.02 %wt and sonicated for another 4-6 hours. In the final stage of sonication, small amounts of the samples were checked for complete QD dispersion with fluorescence microscopy. The mixture is held at 40 $^{\circ}\text{C}$ and then placed in a vacuum oven and slowly cooled overnight, which drives the assembly of the NPs.

For TEM co-assembly samples, 0.2 μL of the mixture is deposited directly onto Au lacey carbon TEM grids (400 mesh, Ted Pella Inc). Excess solvent is wicked away with a Kim wipe and the samples are allowed to cool slowly in an oven. Similar samples can be prepared by letting 20 μL of the mixture cool in a centrifuge tube and after the process is complete, following the same deposition procedure. As the samples are predominantly LC, there is no need to allow time for drying, as there is no solvent left to evaporate.

5.2.2 Ring-like nanoparticle co-assembly preparation

We prepare co-assemblies with ring-like structures for scanning PL by depositing 5 μL of the mixture onto a glass slide pre-coated with polyvinyl alcohol (Sigma Aldrich) which is rubbed uniformly with velvet to induce a planar alignment of the 5CB. A glass slide is also coated the same way and placed on top. For homeotropic alignment, glass slide and cover slip are dipped in a 5 μM solution of cetyltrimethylammonium bromide (CTAB) and water. The mixture and glass are held at 40 $^{\circ}\text{C}$ and then placed on a Linkham LTS350 hot-stage and then rapidly cooled to 2 $^{\circ}\text{C}$ above the nematic transition temperature. The samples are then cooled at 0.1 $^{\circ}\text{C min}^{-1}$ while closely following both bright field and cross-polarized microscopy. When a change in LC phase is seen, the temperature is held fixed for 5 – 10 minutes. After the sample settles in a biphasic state, cooling is resumed. This typically occurs twice per 0.1 $^{\circ}\text{C}$, for \sim 0.2 $^{\circ}\text{C}$ until the transition to the nematic phase is complete.

5.2.3 Experimental methods

Transmission electron aberration-corrected microscopy (TEAM) imaging is performed using the TEAM I microscope (<1 nm resolution) in Lorentz mode at Lawrence-Berkeley National Labs (LBNL) at 300 keV. For application of the magnetic field, the samples are tilted to 20 $^{\circ}$ and the field is applied using the objective lens parallel to the beam direction. EDS imaging is performed with a CM 200 TEM machine set to diffraction mode operating at 200 keV. Upright microscopy is performed using a Leica DM2500P equipped with a Q-image Retiga camera. Scanning PL is performed by exciting the samples on a glass slide using a continuous wave CUBE laser (409 nm, with a diffraction limited spot size of approximately 0.5 μm) and collected with an Acton 300i spectrometer dispersed onto a thermo-electrically cooled CCD camera (resolution \sim 0.18 nm). The samples are placed on a high-resolution ESP 300 motorized scanning stage.

5.3 Results and discussion

5.3.1 Assembly and structural imaging of nano-composites

Pure 5CB is a thermotropic LC which transitions from the isotropic phase into the nematic phase at 34.1 $^{\circ}\text{C}$. The nematic LC mesophase is where the anisotropic rod-like molecules are oriented along their director axis, defined by a vector that points along their long axis. 5CB serves to both assemble the NPs and stabilize the co-assemblies post assembly. First, the NPs need to be dispersed throughout the LC to

allow for optimal directed assembly, and this is done by heating the LC into the isotropic phase ($\sim 40\text{ }^{\circ}\text{C}$) and sonicating. Better results arise the more evenly dispersed the NPs become, and this can be checked via optical microscopy with a small amount of sample before sonication completes. Then, the mixture is very slowly cooled through the transition temperature at $\sim 0.1\text{ }^{\circ}\text{C min}^{-1}$. The nematic phase is a poorer solvent for the NPs than the isotropic phase. As islands of nematic phases develop, NPs are gradually expelled into the isotropic phase to minimize the elastic deformation energy cost, and finally end up in defect points when the LC transition is complete. The transition temperature is $\sim 34.8\text{ }^{\circ}\text{C}$ when 5CB is doped with $\sim 0.06\text{ }\%$ wt of NPs. We will start by investigating the behavior of such a process at the nanoscale using TEM.

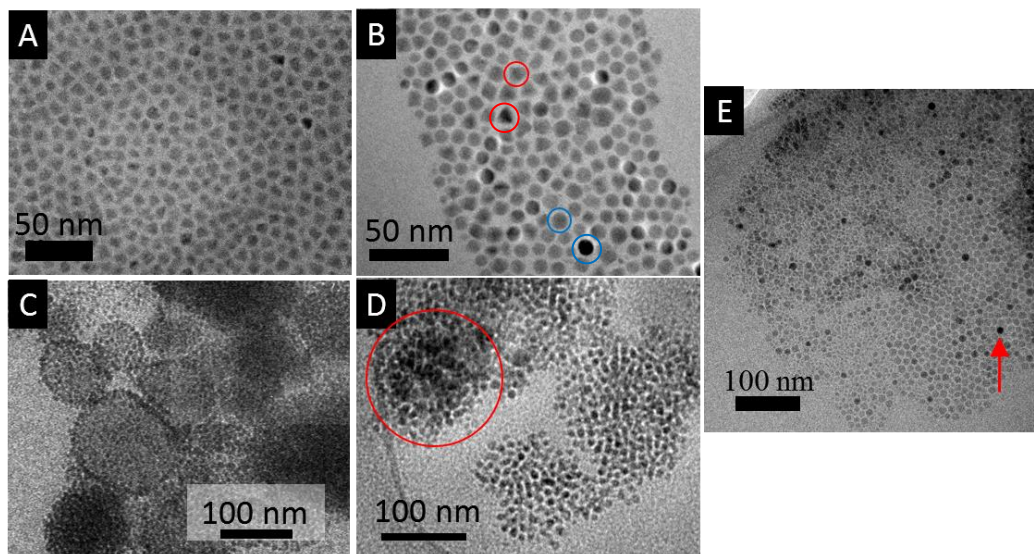


Figure 1. A) QD dropcast B) MNP/QD dropcast C) MNP/QD co-assembly in LC showing rings at the nano-scale D) Co-assembly in LC with monolayer and multi-layer which will be used later in paper for elemental analysis E) MNP only in LC

Fig. 1a shows dropcast QDs without LC on a TEM grid. Fig. 1b shows dropcast of both MNPs and QDs without LC. Both of these dropcast samples were prepared as stated in the experimental section. During evaporation of the toluene solvent, the NPs close-pack in monolayers. Both samples exhibit very similar close-packing behavior and preferentially form monolayers. Comparing Fig. 1a and Fig. 1b, the QDs (red circle Fig. 1b) are faceted in shape and significantly less spherical than the MNPs (blue circle Fig. 1b). Additionally, the circles compare QDs close to Bragg alignment (darker) and further away (more gray). Likewise, the blue circles compare a dark MNP close to Bragg alignment to a MNP further from the Bragg angle. Fig. 1c shows co-assemblies in LC that were formed in a centrifuge tube and then deposited on a TEM grid. The thinnest aggregates of NPs, one to two layers) allow electrons to pass through, and the thicker clusters scatter electrons significantly or completely and appear dark grey or black. The LC molecules are often difficult to be seen separately from the lacey carbon (C) backbone of the TEM grid, except where the LC layer is very thick (approximately 100 nm). Fig. 1d shows a co-assembly formed on a TEM grid and is very similar in structure to the sample in Fig. 1c. These samples both show varying thickness. Most often, when using both QDs and MNPs, the assemblies form in multiple layers causing the image to appear darker. One such example is shown in the red oval in Fig. 1d. The increased presence of LC in these formations also darken the area. They have an ellipsoidal and sometimes circular nature. Some areas, while less common, are a single layer of NPs and can be seen in the bottom right of Fig 1d. While the formations vary in size, the inter-particle separation is uniform throughout as we demonstrate

in SAXS data from our previous paper [9]. The most apparent difference in Fig. 1c-d is the presence of a pronounced edge (ring) at the edges of the co-assemblies in Fig. 1c, as a result of more NPs at the edges, and this difference will be discussed in greater detail in the following two sections of this paper. Fig. 1e shows assemblies consisting of MNPs in LC without QDs. By using only MNPs, the LC phase transition assembles the NPs more regularly in single NP layers. In addition, the areas with multiple layers still tend to aggregate but much less so in ellipsoidal or circular formations. By comparing samples with both types of NPs and just MNPs, it appears as though iron-oxide NPs are much more likely to form these single layers of NPs, in other words, much more likely to disperse. But, there are thicker regions which can be seen at the far right of Fig. 1e similar to using LC to direct the assembly of MNPs and QDs. We posit this increased tendency to form single layers is due to iron-oxide inter-particle interactions both with each other and the lacey C of the TEM grid. This method also produces a clearer contrast with NPs that have that Bragg angle aligned for maximum scattering of electrons highlighted in Fig. 1e by a red arrow. The reason for this is likely due to MNPs more preferentially scatter electrons than QDs, and so the apparent contrast between a MNP close to Bragg alignment appears significantly darker. Now that we have done extensive TEM imaging of NPs assembled in LC, a more complete picture of their structure has emerged. Each individual large cluster, eg the entirety of Fig. 1c-d, is made of many smaller clusters. In contrast to a fractal-like model in our previous work, each individual cluster is much more ordered than previously believed.

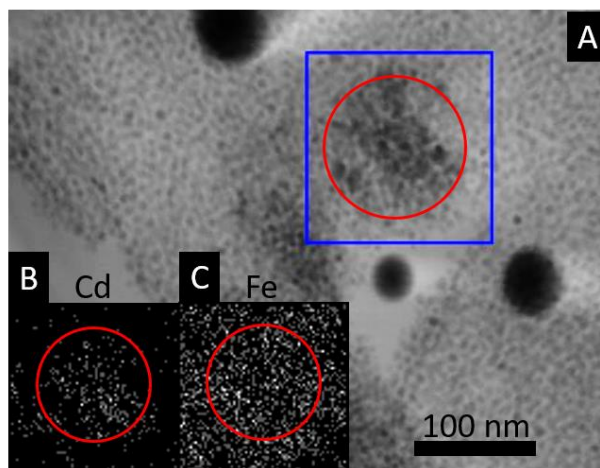


Figure 2. A) Inverted TEM image of area to be scanned with STEM/EDS in diffraction mode. B) EDS images showing location of Cd element and C) location of Fe element.

To further investigate the structural characteristics of the co-assemblies we look to energy dispersive X-ray spectroscopy (EDS) for elemental information to investigate what changes when using the two types of NPs in LC. Fig. 2a shows a TEM image in diffraction mode of a sample area similar to Fig. 1d. The image has been inverted to compare easily. Diffraction mode is used for scanning TEM (STEM) from which we can obtain EDS for elemental information. In Fig. 2a, the area scanned is the blue square, and the red circle highlights an area where there is a multi-layer assembly of NPs. Fig. 2b shows the location of the Cd element, indicative of the presence of QDs. Fig. 2c shows Fe element, indicative of MNPs. The red circle helps compare the same location between the three figures. Comparing the TEM image with the EDS images, it can be seen that the QDs are predominantly located within the red circle which is more than one layer of NPs, while MNPs disperse more, akin to the behavior shown in Fig. 1e of MNPs only in LC. The ligands of both NPs consist of long hydrocarbon chains and the main difference is the functional group that terminates the ligand and bonds to the NPs. Due to their overall similarity, the

difference in assembly behavior of the NPs in LC is most likely due to the elemental nature of the NP cores themselves.

From the ring-like edges seen in Fig. 1c, and the knowledge that the MNPs like to disperse more readily as seen in Fig. 2, seem to indicate that the MNPs themselves can disrupt the LC nematic phase formation in such a way that we can make novel structures that are not possible by using just QDs in LC. We aim to take advantage of this knowledge by generating ring-like microstructures have a different structure than close-packed, uniform clusters of NPs and this will be the purpose of the next section.

5.3.2 Assembly of ring-like microstructures

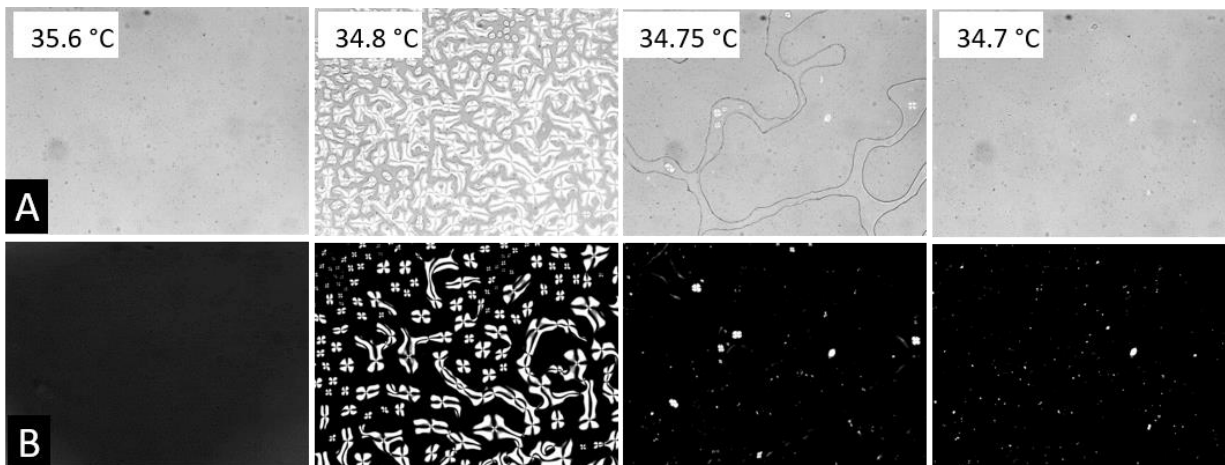


Figure 3. Co-assemblies in homeotropically-aligned LC. A) Bright field microscopy demonstrating the cooling procedure. B) Corresponding cross-polarized imaged of A.

In previous work, the LC phase transition from isotropic to nematic was used to form compact QD clusters [9]. In addition, we have previously reported co-assemblies in LC generated via the same procedure that exhibit an induced brightening of the QDs in the presence of an external magnetic field [10]. One exciting way to take advantage of the co-assembly formation procedure is to make a small change in the cooling procedure to generate clusters of NPs with ring-like halos surrounding them. This was first observed as a result of taking microscope images while holding the sample temperature fixed and we noticed the clusters change from closely-packed aggregates to clusters surrounded by rings. Additionally, the presence of MNPs seems to disrupt the LC phase more aggressively as the iron oxide cores prefer to disperse much more so than the QDs. Fig. 3a-b shows the cooling procedure via upright microscopy used to consistently generate ring-like structures in homeotropically-aligned LC, in which the nematic phase is aligned perpendicular to the glass slide surface (out of the page). Samples were prepared as detailed in the experimental section and isotropic-nematic transition temperature was determined to be 34.8 °C. The sample was cooled to just above the transition temperature, 35.6 °C, and then cooled at 0.1 °C min⁻¹. The LC phase transition was tracked via bright field (top row, Fig. 3a) and cross-polarized microscopy (bottom row, Fig. 3b). At 35.6 °C, the LC is still in the isotropic phase and the NPs are well dispersed after the sonicating bath. There is no residual solvent. As the sample is cooled at a rate of 0.1 °C min⁻¹, the nematic phase starts to form at 34.8 °C (grey regions in Fig. 3a, black regions Fig. 3b). The important assembly step that creates ring-like co-assemblies is performed by leaving the sample fixed at this temperature for 10 minutes. Theoretically, in pure 5CB, at this point the entire sample would transition to nematic and appear dark, as that would be the lowest free energy state for the LC matrix.

However, due to the presence of NPs, and especially two types of NPs with their difference in assembly behavior, the system settles in a biphasic state. Nanoparticles tend to favor the isotropic semi-ordered phase over well-ordered nematic phase and thus phase separate. In the white regions, the LC director is disordered and fluctuates in appearance (the white clover-like regions move around) because there is no proper director. Inside these regions, the LC is isotropic. On the boundary of isotropic and nematic, the LC molecules are aligned in one direction, which is why the image appears white under cross-polarizers. The director of the LC molecules immediately outside the boundary have a different alignment than the total matrix, which is why the image appears bright, despite the fact that the inside region is isotropic and should appear dark. If Fig. 3 was a video and not a still image, these clover-like structures would be constantly changing. Once the quasi-stable state has remained for ~ 10 minute, the sample is allowed to cool again. At ~ 34.75 °C, the sample is again held for 10 minutes at this temperature, and the nematic regions make up the significant portion of the image, with the shrinking isotropic regions appearing like snake-like patterns, and are easily seen in Fig. 3a. It is the expanding phase front of the LC that drives the assembly of the NPs into lines, seen as the darker lines at the boundary of the nematic and isotropic phase. By fixing the sample temperature for 10 minutes, the NPs are assembled in these lines and some NPs have a tendency to stay there, causing ring-like structures surrounding the normal, closely packed clusters of NP. Finally, the sample is again slow cooled and the NPs end up clustered in defect regions after the phase transition is complete at 34.7 °C. At this scale, the rings are not readily, visible. However, at higher magnification, the rings resulting from this process can be seen clearly and are shown in Fig 4a. The process also yields rings when using 5 nm MNPs and are shown in Fig 4b. This is important to note because the EDS image in Fig. 2 suggests that the two types of NPs generate the ring-like co-assemblies due to elemental composition and not because of the size mismatch between the MNPs and QDs. Additionally, we performed confocal fluorescence microscopy to obtain a better look at the ring-like co-assemblies.

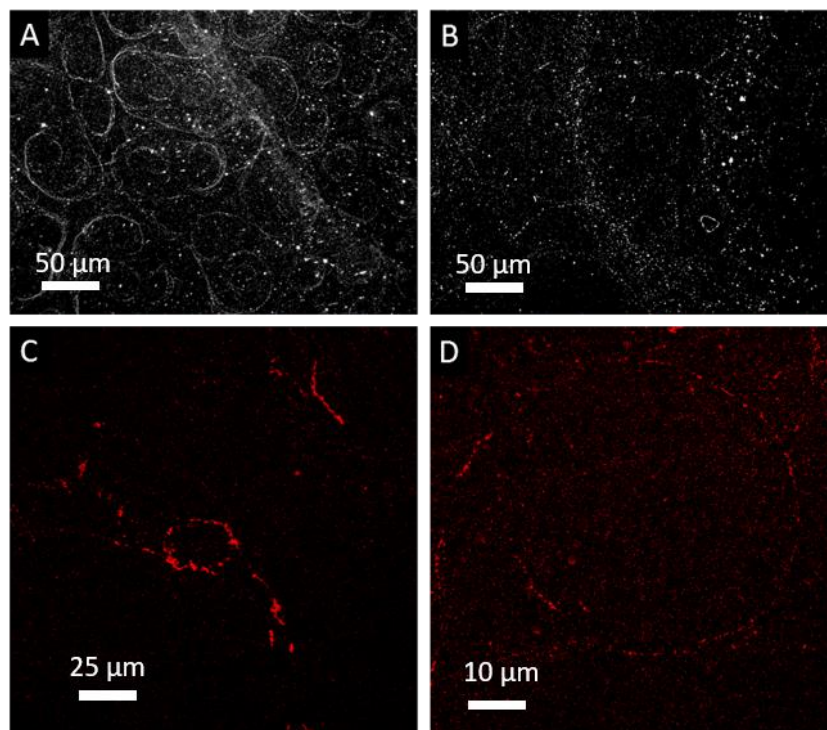


Figure 4. A) Fluorescence microscopy of co-assemblies, QD “lines” and rings generated with new cooling procedure. B) Same assembly procedure with 5nm MNPs and QDs. C) and D) Confocal microscopy of ring-like regions from the sample shown in A.

5.3.3 Synergistic emission enhancement in nano-composites

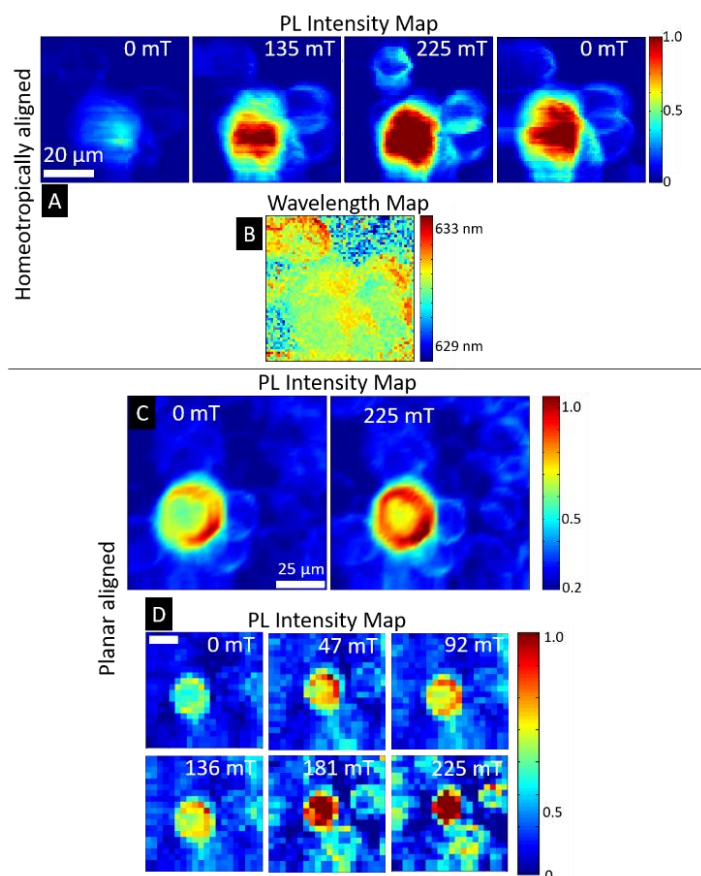


Figure 5. A) PL Intensity map of homeotropically aligned LC directed assembly of MNPs and QDs showing PL enhancement with applied magnetic field B) Wavelength map of corresponding assembly C) PL intensity of planar aligned, comparable to sample shown in a D) PL enhancement, planar aligned. Scale

We aim to take advantage of the ring-like co-assemblies by examining their behavior in an applied external magnetic field. To show this, we track PL enhancement systematically with increasing magnetic field. Fig. 5a shows a co-assembly in homeotropically aligned LC which exhibits PL enhancement with the application of an applied magnetic field. As the field is applied, up to 225 mT, there is an induced brightening of the QDs which leads to a 2-3 fold increased PL intensity. This effect happens within the cluster, but also within the surrounding ring-like structures. When the external field is returned to zero, the effect is partially reversible, returning to a PL state similar to the 135 mT image. Fig. 4b shows a wavelength map of the same cluster. Due to FRET, there is a greater redshift of the QDs in the ring-like regions, indicating that the QDs are more closely-packed in these regions. This may indicate the NPs are preferentially pushed to the snake-like regions shown in Fig. 3a and Fig. 4, and assemble more densely in these lines. Fig. 5c-d show these assemblies in planar aligned LC (the LC director aligned along the glass slide, parallel to the page) which also exhibit brightening with a systematically increased applied external magnetic field. Fig. 4c shows the most notable effect of preferential brightening on the edges of the clusters. The effect happens in co-assemblies made with either planar and homeotropically aligned LC. This indicates that it is the MNPs responsible for the observed brightening and not the re-alignment of the LC with the external field because the Fredericks transition for pure 5CB is approximately 590 mT

and is a thresholding effect. The magnetic fields used here are well below this value. Also, the PL enhancement is not the result of a photo-induced magnetic effect on the QDs, as previous papers on this type of QD have shown this requires a substantially larger field (~ 2 T) to cause a noticeable effect in QD PL [10]. Now that these co-assemblies surround by ring-like structures show PL brightening in an external field as seen in our previous work, we would like to understand the mechanism responsible for this behavior. To do so, we require a much closer look at what can possibly be happening, and the scale mismatch of optical microscopy in the behavior of NPs is too great. We return to TEM imaging, specifically Lorentz TEM, to investigate the mechanism which may be responsible for the reorganization and subsequent PL enhancement of these co-assemblies.

5.3.4 Magnetic nanoparticle rotation at the nano-scale

We investigate the behavior of only MNPs in LC at the nano-scale under the presence of an applied field to further understand the behavior of these systems. The TEAM I microscope was set to Lorentz mode to allow the application of a magnetic field without changing the focus. Then, the sample was tilted 20° and a 200 mT field was applied by using the objective lens, which is the maximum external field possible. The reason the sample was tilted is that the external magnetic field is applied out of the sample and by rotating the sample, it allows for MNPs to experience a greater inter-particle interaction generating a stronger attractive force, similar to the North and South ends of two magnets stacked on top of each other. Finally, 20° is the sample tilt used to collect EDS images. To understand the basics of the upcoming Lorentz TEM images, the schematic in Fig. 6 shows a model of a MNP at a random rotation and subsequent rotation to align the magnetic easy-axis along the applied magnetic field. The blue arrow in Fig. 6a represents the Bragg angle orientation for maximum scattering of the electron beam, causing the MNP to appear black in a TEM image. As the MNPs were dropcast, the magnetic easy axis is in a random orientation and is shown by the red arrow. When an external field is applied, the MNP rotates slightly to align its magnetic easy axis along the field and minimize energy. Because the orientation for maximum scattering is not the same as the orientation required to minimize magnetic energy, applying a field results in the MNP rotating away from the Bragg angle and thus appearing grey (Fig. 6b) in TEM images.

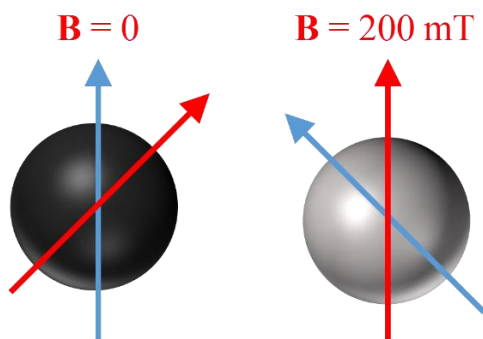


Figure 6. Schematic of a MNP before and after application of an external magnetic field. A) MNP with Bragg angle (blue arrow) aligned for maximum scattering causing the particle to appear dark in TEM images. B) With a 200 mT applied field, the MNP rotates its magnetic easy axis (red arrow) along the field, causing the Bragg angle to rotate away from the angle required for maximum scattering, causing the particle to appear grey.

Fig. 7a shows MNP that have been drop-cast onto a TEM without LC as a control via the procedure in the experimental section. By examining the contrast of the MNPs, we know that the darker ones indicate their Bragg angle is aligned to the maximum scattering angle. Fig. 7b shows the sample after an applied 200 mT external magnetic field. The MNPs that have rotated significantly from Fig. 7a are highlighted by red and blue circles. Some of them have rotated toward the Bragg angle for maximum scattering and are darker (red circles), and some have done the opposite, appearing more grey (blue circles). This seems to indicate that the MNPs that can freely rotate are doing so randomly by the energy of the electron beam. Many of the MNPs do not move, and this is likely due to an interaction between the TEM grid surface and the NPs themselves, preventing any rotation.

However, the results of MNP assembled by the LC thermotropic phase transition (detailed in the experimental section) are very different. In the presence of an external magnetic field of 200 mT, almost all MNPs that change contrast significantly do so by decreasing in intensity (blue circles, Fig. 7b), as opposed to some getting darker, and some getting brighter when there is no LC matrix. This is most likely due to the fact that the MNPs are surrounded by LC and thus are more free to rotate, aligning the easy axis of their magnetic anisotropy along the field, and this orientation is not the angle for maximum electron scattering. It is this rotation that is the most likely candidate for the mechanism responsible for enhancing the local field and causing spatial reorganization of the co-assemblies, resulting in the observed PL enhancement. The MNPs rotate to align their easy axis with the applied external magnetic field, and in doing so, their ensemble net magnetization increases, allowing for a greater ease of rotation within the LC matrix. Because there are so many NPs in Fig. 7, we perform a statistical analysis of these samples to greater expose the difference between MNPs along and MNPs in LC.

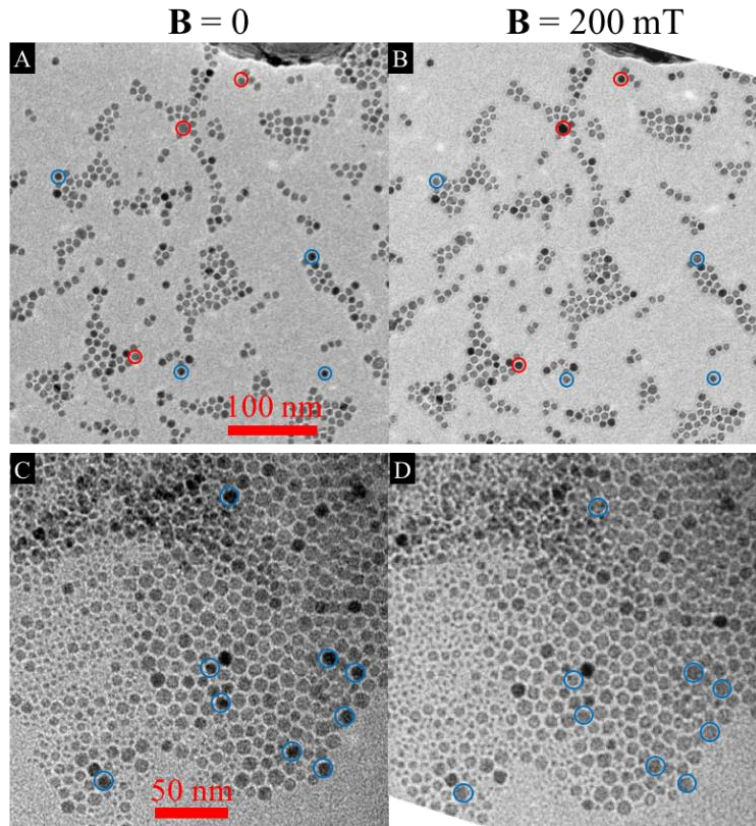


Figure 7. A) Drop-cast MNPs viewed with Lorentz mode TEM. B) 200 mT applied magnetic field using the objective lens in Lorentz mode. C) MNP in 5CB viewed in Lorentz mode TEM. D) 200 mT applied field. In all four images, red circles highlight MNPs that have rotated closer to Bragg angle, blue circles highlight MNPs that have rotated away from Bragg angle.

We now track the intensity of the NPs in Fig. 7 to verify that the LC matrix allows for the MNPs to rotate in a controllable fashion. To do this, we perform imageJ analysis of the mean grey value within a MNP. MNPs that are close to the Bragg angle will have a low value, and the brighter MNPs will be further away. The values range from approximately 60-140 counts for Fig. 7a-b, and 90-130 for Fig 7c-d. Fig. 8a-b are the histograms corresponding to Fig. 7a-b. Looking at the most common grey value of 125 counts, the surrounding values of 115 and 135 counts smooth out like one would expect for random rotation of the MNPs. Some of the MNPs are rotating away from the Bragg angle, and some are rotating toward. This is common for NPs in the presence of the energetic electron beam. Fig. 8c-d are the histograms corresponding to Fig 7c-d. This trend shows an overwhelm reduction in the number of darker MNPs, indicative of MNPs aligning with the magnetic field and thus reducing their contrast. In both samples, some MNPs are fixed, and do not change or less likely rotate and then rotate back to where they started, or rotate 180° or rotate azimuthally. What is clear is that the LC matrix allows for more of a controlled rotation of the MNPs, and that the alignment that minimizes their magnetic energy is not the same as the Bragg angle orientation for maximum scattering.

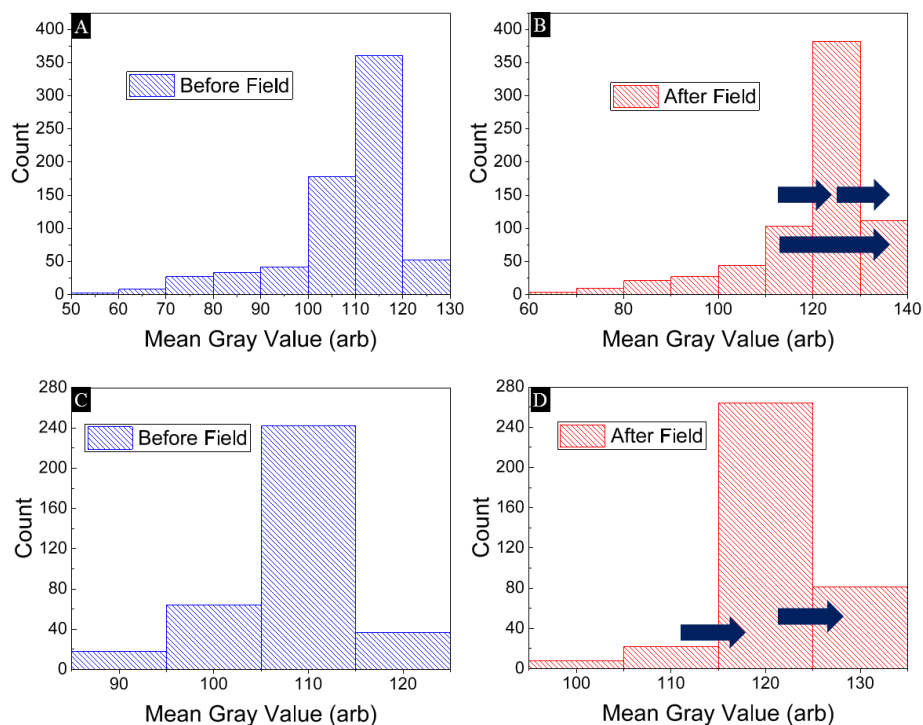


Figure 8. A) Histogram of drop-cast MNPs corresponding to Fig. 7a B) Histogram of MNPs after 200 mT applied magnetic field. This shows a trend of random rotation. C) Histogram MNP in 5CB corresponding to image in Fig. 7c. D) Histogram of MNPs after 200 mT applied field. This shows a trend of an overall brightening of MNPs.

5.4 Conclusion

We assembled QDs and MNPs in a LC matrix and performed elemental analysis at the nano-scale and found that the iron oxide NPs tend to aggregate less preferentially than the QDs, most likely due to elemental composition and not due to size or surface characteristics. This led to a modification to the cooling process in which we halt the LC in a biphasic state to generate ring-like structures in addition to co-assembly clusters. The sensors exhibit an induced brightening in the presence of small external magnetic fields, indicating that the MNPs must aid in the spatial reorganization of both the QDs and the LC matrix. To improve our understanding of this behavior, we probed the directed assembly of MNPs in LC at the nano-scale, showing that one can rotate the MNPs in a magnetic field controllably. This indicates that at the micro-scale, the application of an external magnetic field causes structural reorganization of the MNPs by which their net magnetization increases. This in turn causes the LC material to respond more strongly to the applied field and finally causes the co-assemblies to spatially reorganize and exhibit an increase in photoluminescence (PL) intensity. Furthermore, as these samples are assembled in a fluid medium, they may lead the way to improving fluid-based applications. Finally, because the rings are smaller in both area and volume, this potentially could be used to create smaller magnetic field sensors.

The next step is getting the MNPs to move across the TEM grid laterally, not simply rotating in place. The controlled rotation is an excellent step toward making this happen, indicating that spatial

reorganization may be realized. With modifications to the LC matrix, and NP surface modification, further synthesis and testing may allow these sensors to further push the possibility of fluid-based processing.

6 Conclusion

We started by investigating a ligand exchange on QDs to improve their robustness under ambient conditions for use in devices containing ensembles of QDs. This occurred because the large, LC-like ligands kept the interdot spacing at approximately 1 nm further apart than close-packed QDs. In addition, the LC-like ligands increase charge separation from the core of the QD, further stemming photo-oxidation. Ultimately, this became a way to increase the color stability of a QD ensemble, which is ideal for any application where the QD emission is tuned to maximize the output of the device.

We have also demonstrated that a thermotropic LC can be used to form co-assemblies that exhibit a photoluminescence (PL) brightening under the application of small magnetic fields. These sensors brighten in such a way that can be calibrated to act as a novel, all-optical device. Initially, we proposed a mechanism in which the MNPs cause the LC molecules to locally realign, and thus compact the clusters increasing the density of QDs which leads to PL brightening. It is important to note that this compaction happens without decreasing the interdot spacing, but rather the fractal like nature of these co-assemblies compacting. However, this picture may not be totally complete so we investigated the interaction between the three components (QDs, MNPs, and LC molecule) at the nanoscale. This demonstrated that the MNPs are allowed to spatially rotate in the presence of an external magnetic field due to the LC matrix they exist in, and this rotation leads to a larger local magnetic field. It is then likely that this increase in net magnetization is responsible for the change in LC alignment that is responsible for the increase in density of QDs per unit area.

One fundamental advantage to the magnetic sensors is the potential for a nano-lab. In other words, it is possible to modify them to study fundamental physics, like the Ising model, by using MNPs themselves and not computer simulations or theory. This could lead to an increased understanding of MNP ensembles and magnetic phenomena.

One way to improve these sensors is to not only make them smaller, but also understand and control the nanoscale interactions between the MNPs, QDs, and LC molecules. I propose that combining two types of LC molecules, 8CB and 5CB, could allow for creating suspended films doped with NPs. By keeping the NPs suspended, they would not be allowed to interact with the sample surfaces. As explained in chapter 5, the MNPs are particularly prone to dispersing and fixing to the sample cell walls. If we were able to increase the number of MNPs that spatially rotate, the net magnetization would also increase, allowing for smaller, more sensitive magnetic field sensors. Furthermore, we only examined 5 and 10 nm MNPs and 7 nm QDs. It is very likely that other combinations of MNPs and QDs could improve these sensors and provide a greater understanding as to how they work. In fact, we are not limited to iron oxide and CdSe NPs. There are many, many choices which may prove more reproducible and more sensitive.

The study of these sensors outlined in this thesis lead toward several exciting and novel research outcomes. The ability to manipulate NPs in LC can lead to excellent versatility in which the NP ensemble behavior be changed post-synthesis. For example, as mentioned earlier, inter-particle spacing within an ensemble of MNPs changes their interactions, and it may be possible to have one device act paramagnetically for reading and writing of data, and then ferromagnetically for information storage. Furthermore, combining MNPs with QDs could lead to the ability for both data storage and information processing by the QDs by taking advantage of the spin properties of an excited electron. One day, by combining this fundamental information of NPs with the LC matrix itself, the goal of fluid-based processing may be realized.

References

Chapter 1 References

- [1] Y. Sun, M. B. Salamon, K. Garnier and R. S. Averback, Memory effects in an interacting magnetic nanoparticle system, *Phys. Rev. Lett.*, **91**, 167206, 2003.
- [2] Mrinmoy De, Partha S. Ghosh and Vincent M. Rotello, Applications of nanoparticles in biology, *Adv. Mater.*, **20**, 4225, 2008.
- [3] A. J. Nozik, M. C. Beard, J. M. Luther, M. Law, R. J. Ellingson, and J. C. Johnson, Semiconductor quantum dots and quantum dot arrays and applications of multiple exciton generation to third-generation photovoltaic solar cells, *Chem. Rev.*, **110**, 6873, 2010.
- [4] M. Nirmal, L. Brus. Luminescence Photophysics in Semiconductor Nanocrystals. *Accounts of Chemical Research*, **32 (5)**, 407-414, 1999.
- [5] A. P. Alivisatos. Semiconductor Clusters, Nanocrystals, and Quantum Dots. *Science*, **271** 5251, 933-937, 1996.
- [6] Nae-Man Park, Tae-Soo Kim, and Seong-Ju Park. Band gap engineering of amorphous silicon quantum dots for light-emitting diodes. *Appl. Phys. Lett.*, **78**, 2575-2577, 2001.
- [7] Lei Zhuang, Lingjie Guo, and Stephen Y. Chou. Silicon single-electron quantum-dot transistor switch operating at room temperature. *Appl. Phys. Lett.*, **72**, 1205-1207, 1998.
- [8] A. J. Nozik. Quantum dot solar cells. *Physica E*, **14**, 115-120, 2002.
- [9] P. Majewski, B. Thierry. Functionalized Magnetite Nanoparticles—Synthesis, Properties, and Bio-Applications. *Critical Reviews in Solid State and Materials Sciences.*, **32:3-4**, 203-215, 2007.
- [10] H. Sahoo. Förster resonance energy transfer – A spectroscopic nanoruler: Principle and applications. *Journal of Photochemistry and Photobiology C: Photochemistry Reviews*. **12**, 20-30, 2011.
- [11] B. O. Dabbousi, J. Rodriguez-Viejo, F. V. Mikulec, J. R. Heine, H. Mattoussi, R. Ober, K. F. Jensen, M. G. Bawendi. (CdSe)ZnS Core–Shell Quantum Dots: Synthesis and Characterization of a Size Series of Highly Luminescent Nanocrystallites. *The Journal of Physical Chemistry B*, **101 (46)**, 9463-9475, 1997.
- [12] C. R. Kagan, C. B. Murray, M. Nirmal, M. G. Bawendi. Electronic Energy Transfer in CdSe Quantum Dot Solids. *Phys. Rev. Lett.*, **76**, 1517, 1996.
- [13] T. Pons, I. L. Medintz, K. E. Sapsford, S. Higashiya, A. F. Grimes, D. S. English, H. Mattoussi. On the Quenching of Semiconductor Quantum Dot Photoluminescence by Proximal Gold Nanoparticles. *Nano Letters*. **7 (10)**, 3157-3164, 2007.
- [14] I. Liu, H. Lo, C. Chien, Y. Lin, C. Chen, Y. Chen, et al. Enhancing photoluminescence quenching and photoelectric properties of CdSe quantum dots with hole accepting ligands. *J. Mater. Chem.* **18**, 675-682, 2008.
- [15] G. V. Shcherbatyuk, R. H. Inman, S Ghosh. Anomalous photo-induced spectral changes in CdSe/ZnS quantum dots. *Journal of Applied Physics.*, **110**, 053518, 2011.
- [16] D. J. Griffiths. *Introduction to Electrodynamics*, 3rd ed., p. 278. 1999.
- [17] C. Kittel. *Introduction to Solid State Physics*, 3rd ed. Wiley, 2005.
- [18] D. Chandler. *Introduction to Modern Statistical Mechanics*. Oxford University Press, p. 120, 1987.
- [19] S. Bedanta, W. Kleeman. *Supermagnetism. J. Phys. D: Appl. Phys*, 2009, **42**, pp 28.
- [20] Balents, Leon. Spin Liquids in Frustrated Magnets. *Nature*, **464.7286**, pp 199-208, 2010.
- [21] B. Aslibeiki, P. Kameli, H. Salamati, M. Eshraghi, T. Tahmasebi. Superspin glass state in MnFe₂O₄ nanoparticles. *Journal of Magnetism and Magnetic Materials*, **322 (19)**, 2929-2934, 2010.

- [22] N. Bao, A. Gupta. Soft-assembly of superparamagnetic nanoparticles. *J. Mater. Res.*, **26** (2), 111-121, 2011.
- [23] C. Djurberg, P. Svedlindh, and P. Nordblad, M. F. Hansen, F. Bødker, and S. Mørup. Dynamics of an Interacting Particle System: Evidence of Critical Slowing Down. *Phys. Rev. Lett.*, **79**, pp 5154–5157, 1997.
- [24] T. Jonsson, P. Svedlindh, M. F. Hansen. Static Scaling on an Interacting Magnetic Nanoparticle System. *Phys. Rev. Lett.*, **81**, 3976–3979, 1998.
- [25] S. I. Fullem. Study of Superspin-glass Effect and Superparamagnetic Behavior in Magnetite Nanoparticles. Proquest Information and Learning Co., 2006.
- [26] Y. Sun, M. B. Salamon, K. Garnier, R. S. Averback. Memory Effects in an Interacting Magnetic Nanoparticle System. *Phys. Rev. Lett.*, **91** (16), 2003.
- [27] P.G. de Gennes, J. Prost. *The Physics of Liquid Crystals*, 2nd ed. Oxford University Press, 2003.
- [28] K. S. Leschkies, R. Divakar, J. Basu, E. Enache-Pommer, J. E. Boercker, C. B. Carter, U. R. Kortshagen, D. J. Norris, E. S. Aydil. Photosensitization of ZnO Nanowires with CdSe Quantum Dots for Photovoltaic Devices. *Nano Letters*, **7** (6), 1793-1798, 2007.
- [29] R. Beaulac, P. I. Archer, X. Liu, S. Lee, G. M. Salley, M. Dobrowolska, J. K. Furdyna, D. R. Gamelin. Spin-Polarizable Excitonic Luminescence in Colloidal Mn²⁺-Doped CdSe Quantum Dots. *Nano Letters*, **8** (4), 1197-1201, 2008.
- [30] J. J. Peterson, T. D. Krauss. Fluorescence Spectroscopy of Single Lead Sulfide Quantum Dots. *Nano Letters*, **6** (3), 510-514, 2006.
- [31] Q. A. Pankhurst, J. Connolly, S. K. Jones, J. Dobson. Applications of magnetic nanoparticles in biomedicine. *J. Phys. D: Appl. Phys.*, **36**, R167, 2003.
- [32] B. D. Terris, T. Thomson. Nanofabricated and self-assembled magnetic structures as data storage media. *J. Phys. D: Appl. Phys.*, **38**, R199, 2005.
- [33] Kim, J., Kim, H., Lee, N., Kim, T., Kim, H., Yu, T., Song, I., Moon, W. and Hyeon, T. Multifunctional Uniform Nanoparticles Composed of a Magnetite Nanocrystal Core and a Mesoporous Silica Shell for Magnetic Resonance and Fluorescence Imaging and for Drug Delivery. *Angewandte Chemie International Edition*, **47**, 8438–8441, 2008.
- [34] P. Kopčanský, N. Tomašovičová, M. Koneracká, M. Timko, V. Závišová, A. Džarová, J. Jadzyn, E. Beaunon, X. Chaud. Phase Transitions in Liquid Crystal Doped with Magnetic Particles of Different Shapes. *International Journal of Thermophysics*, **32** (4), 807–817, 2011.
- [35] S. V. Burylov and Y. L. Raikher, Magnetic Fredericksz transition in a ferronematic, *J. Magn. Magn. Mater.*, **122**, 62, 1993.
- [36] F. Capolino. *Applications of Metamaterials*. Taylor & Francis Group, LLC, 2010.
- [37] Z. Chen, J. Moore, G. Radtke, H. Sirringhaus, S. O'Brien. Binary Nanoparticle Superlattices in the Semiconductor–Semiconductor System: CdTe and CdSe. *J. Am. Chem. Soc.*, **129** (50), 15702–15709, 2007.
- [38] A. L. Rodarte, F. Cisneros, J. E. Hein, S. Ghosh, L. S. Hirst. Quantum Dot/Liquid Crystal Nanocomposites in Photonic Devices. *Photonics*, **2**, 855-864, 2015.
- [39] J. J. Amaral, J. Wan, A. L. Rodarte, C. Ferr , M. T. Quint , R. J. Pandolfi, M. Scheibner, L. S. Hirst, S. Ghosh. Magnetic field induced quantum dot brightening in liquid crystal synergized magnetic and semiconducting nanoparticle composite assemblies. *Soft Matter*, **11**, 255-260, 2015.
- [40] B. Rožič, J. Fresnais, C. Molinaro, J. Calixte, S. Umadevi, S. Lau-Truong, N. Felidj, T. Kraus, F. Charra, V. Dupuis, T. Hegmann, C. Fiorini-Debuisschert, B. Gallas, and E. Lacaze. Oriented Gold Nanorods and Gold Nanorod Chains within Smectic Liquid Crystal Topological Defects. *ACS Nano*, **11** (7), 6728-6738, 2017.
- [41] Yamada, M.; Shen, Z.; Miyake, M. Self-Assembly of Discotic Liquid Crystalline Molecule-Modified Gold Nanoparticles: Control of 1D and Hexagonal Ordering Induced by Solvent Polarity. *Chem. Commun.*, **0**, 2569–2571, 2006.

- [42] Y. Li, J. J-Y Suen, E. Prince, E. M. Larin, A. Klinkova, H. Thérien-Aubin, S. Zhu, B. Yang, A. S. Helmy, O. D. Lavrentovich, E. Kumacheva. Colloidal cholesteric liquid crystal in spherical confinement. *Nature Comm.*, **7**, 12520, 2016.
- [43] A.E Mahdi, L Panina, D Mapps, Some new horizons in magnetic sensing: high- T_c SQUIDs, GMR and GMI materials, In *Sensors and Actuators A: Physical*, Volume 105, Issue 3, 2003, Pages 271-285.
- [44] Giovanni Rizzi, Jung-Rok Lee, Per Guldberg, Martin Dufva, Shan X. Wang, Mikkel F. Hansen, Denaturation strategies for detection of double stranded PCR products on GMR magnetic biosensor array, In *Biosensors and Bioelectronics*, Volume 93, 2017, Pages 155-160.

Chapter 2 References

- [1] John Kerr. On rotation of the plane of polarization by reflection from the pole of a magnet. *Philosophical Magazine*, **3** (19), 1877.
- [2] J. Cerne. Magneto-Polarimetry Advanced Lab.

Chapter 3 References

- [1] A. M. Smith, H. Duan, M. N. Rhyner, G. Ruan, S. Nie. A systematic examination of surface coatings on the optical and chemical properties of semiconductor quantum dots. *Physical Chemistry Chemical Physics*, **8**, 3895, 2006.
- [2] S. Jeong, M. Achermann, J. Nanda, S. Ivanov, V. I. Klimov, J. A. Hollingsworth. Effect of the Thiol-Thiolate Equilibrium on the Photophysical Properties of Aqueous CdSe/ZnS Nanocrystal Quantum Dots. *J.Am.Chem.Soc.*, **127**, 10126-10127, 2005.
- [3] A. M Smith, H. Duan, M. N. Rhyner, G. Ruan, S. Nie. A systematic examination of surface coatings on the optical and chemical properties of semiconductor quantum dots. *Phys.Chem.Chem.Phys.*, **8**, 3895-3903, 2006.
- [4] F. Xu, L. Gerlein, X. Ma, C. Haughn, M. Doty, S. Cloutier. Impact of Different Surface Ligands on the Optical Properties of PbS Quantum Dot Solids. *Materials.*, **8**, 1858 1870, 2005.
- [5] F. Dubois, B. Mahler, B. Dubertret, E. Doris, C. Mioskowski. A Versatile Strategy for Quantum Dot Ligand Exchange, *J.Am.Chem.Soc.*, **129**, 482-483, 2007.
- [6] K. Susumu, H. T. Uyeda, I. L. Medintz, T. Pons, J. B. Delehanty, H. Mattoussi. Enhancing the Stability and Biological Functionalities of Quantum Dots via Compact Multifunctional Ligands. *J.Am.Chem.Soc.*, **129**, 13987-13996, 2007.
- [7] J. Tang, K. W. Kemp, S. Hoogland, K. S. Jeong, H. Liu, L. Levina, et al. Colloidal-quantum-dot photovoltaics using atomic-ligand passivation. *Nat Mater.*, **10**, 765-771, 2011.
- [8] A. L. Rodarte, F. Cisneros, J. E. Hein, S. Ghosh, L. S. Hirst. Quantum Dot/Liquid Crystal Nanocomposites in Photonic Devices. *Photonics.*, **2**, 855-864, 2015.
- [9] A. L. Rodarte, R. J. Pandolfi, S. Ghosh, L. S. Hirst. Quantum dot/liquid crystal composite materials: self-assembly driven by liquid crystal phase transition templating, *J.Mater.Chem.C.*, **1**, 5527-5532, 2013.
- [10] A. L. Rodarte, Z. S. Nuno, B. H. Cao, R. J. Pandolfi, M. T. Quint, S. Ghosh, et al. Tuning Quantum-Dot Organization in Liquid Crystals for Robust Photonic Applications, *ChemPhysChem.*, **15**, 1413-1421, 2014.
- [11] Z. Lingley, S. Lu, A. Madhukar. A High Quantum Efficiency Preserving Approach to Ligand Exchange on Lead Sulfide Quantum Dots and Interdot Resonant Energy Transfer. *Nano Letters.*, **11**, 2887-2891, 2011.
- [12] Y. Shen, R. Tan, M. Y. Gee, A. B. Greytak. Quantum Yield Regeneration: Influence of Neutral Ligand Binding on Photophysical Properties in Colloidal Core/Shell Quantum Dots. *ACS Nano.*, **9**, 3345-3359, 2015.
- [13] G. V. Shcherbatyuk, R. H. Inman, S. Ghosh. Anomalous photo-induced spectral changes in CdSe/ZnS quantum dots, *Journal of Applied Physics.*, **110**, 053518, 2011.

- [14] X. Mang, X. Zeng, B. Tang, F. Liu, G. Ungar, R. Zhang, et al. Control of anisotropic self-assembly of gold nanoparticles coated with mesogens, *J.Mater.Chem.*, **22**, 11101-11106, 2012.
- [15] W. S. Rasband (<http://imagej.nih.gov/ij/> 1997-2016).
- [16] H. Sahoo. Förster resonance energy transfer – A spectroscopic nanoruler: Principle and applications. *Journal of Photochemistry and Photobiology C: Photochemistry Reviews.*, **12**, 20-30, 2011.
- [17] S. A. Crooker, T. Barrick, J. A. Hollingsworth, V. I. Klimov. Multiple temperature regimes of radiative decay in CdSe nanocrystal quantum dots: Intrinsic limits to the dark-exciton lifetime, *Appl.Phys.Lett.*, **82**, 2793-2795, 2003.
- [18] D. Valerini, A. Creti, M. Lomascolo, L. Manna, R. Cingolani, M. Anni. Temperature dependence of the photoluminescence properties of colloidal CdSe/ZnS core/shell quantum dots embedded in a polystyrene matrix. *Phys.Rev.B.*, **71**, 235409, 2005.
- [19] J. C. Kim, H. Rho, L. M. Smith, H. E. Jackson, S. Lee, M. Dobrowolska, et al. Temperature-dependent micro-photoluminescence of individual CdSe self-assembled quantum dots. *Appl.Phys.Lett.*, **75**, 214-216, 1999.
- [20] E. Lifshitz, I. Dag, I. Litvin, G. Hodes, S. Gorer, R. Reisfeld, et al. Optical properties of CdSe nanoparticle films prepared by chemical deposition and sol-gel methods. *Chemical Physics Letters.*, **288**, 188-196, 1998.
- [21] L. Biadala, B. Siebers, R. Gomes, Z. Hens, D. R. Yakovlev, M. Bayer. Tuning Energy Splitting and Recombination Dynamics of Dark and Bright Excitons in CdSe/CdS Dot-in-Rod Colloidal Nanostructures, *The Journal of Physical Chemistry C.*, **118**, 22309-22316, 2014.
- [22] I. Liu, H. Lo, C. Chien, Y. Lin, C. Chen, Y. Chen, et al. Enhancing photoluminescence quenching and photoelectric properties of CdSe quantum dots with hole accepting ligands. *J.Mater.Chem.*, **18**, 675-682, 2008.
- [23] Z. Nie, A. Petukhova, E. Kumacheva. Properties and emerging applications of self-assembled structures made from inorganic nanoparticles. *Nat Nano.*, **5**, 15-25, 2010.

Chapter 4 references

- [1] S. A. Claridge, J. A. W. Castleman, S. N. Khanna, C. B. Murray, A. Sen and P. S. Weiss, Cluster-assembled materials, *ACS Nano*, **3**, 244, 2009.
- [2] M. Okuda, J.-C. Eloi, S. E. W. Jones, A. Sarua, R. M. Richardson and W. Schwarzacher, Fe₃O₄ nanoparticles: protein-mediated crystalline magnetic superstructures, *Nanotechnology*, **23**, 415601, 2012.
- [3] Y. Zhang, S.-N. Wang, S. Ma, J.-J. Guan, D. Li, X.-D. Zhang and Z.-D. Zhang, Self-assembly multifunctional nanocomposites with Fe₃O₄ magnetic core and CdSe/ZnS quantum dots shell, *J. Biomed. Mater. Res.*, **85A** (3), 840-846, 2007.
- [4] H. Kim, M. Achermann, L. P. Balet, J. A. Hollingsworth and V. I. Klimov, Synthesis and characterization of Co/CdSe core/shell nanocomposites: bifunctional magnetic-optical nanocrystals, *J. Am. Chem. Soc.*, **127**, 544, 2005.
- [5] C. D. Cruz, O. Sandre and V. Cabuil, Phase behavior of nanoparticles in a thermotropic liquid crystal, *J. Phys. Chem. B*, **109**, 14292, 2005.
- [6] B. M. Ross, L. Y. Wu and L. P. Lee, Omnidirectional 3D nanoplasmonic optical antenna array via soft-matter transformation, *Nano Letters*, **11**, 2590, 2011.
- [7] V. Roullier, F. Gasset, F. Boulmedais, F. Artzner, O. Cador and V. Marchi-Artzner, Small bioactivated magnetic quantum dot micelles, *Chem. Mater.*, **20**, 6657, 2008.
- [8] A. Demortie`re, S. Buathong, B. P. Pichon, P. Panissod, D. Guillon, S. Be´gin-Colin and B. Donnio, Nematic-like Organization of Magnetic Mesogen-Hybridized Nanoparticles, *Small*, **6**, 1341, 2010.
- [9] A. L. Rodarte, R. J. Pandolfi, S. Ghosh and L. S. Hirst, Quantum dot/liquid crystal composite materials: self-assembly driven by liquid crystal phase transition templating, *J. Mater. Chem. C*, **1**, 5527, 2013.

- [10] A. Mertelj, D. Lisjak, M. Drofenik and M. Copic, Ferromagnetism in suspensions of magnetic platelets in liquid crystal, *Nature*, **504**, 237, 2013.
- [11] D. F. Gardner, J. S. Evans and I. I. Smalyukh, Towards reconfigurable optical metamaterials: colloidal nanoparticle self-assembly and self-alignment in liquid crystals, *Mol. Cryst. Liq. Cryst.*, **545**, 1227, 2011.
- [12] T. Dietl, A ten-year perspective on dilute magnetic semiconductors and oxides, *Nat. Mater.*, **9**, 965, 2010.
- [13] J. J. Vallooran, R. Negrini and R. Mezzenga, Controlling anisotropic drug diffusion in lipid-Fe₃O₄ nanoparticle hybrid mesophases by magnetic alignment, *Langmuir*, **29**, 999, 2010.
- [14] V. Salgueiriño-Maceira, M. A. Correa-Duarte, M. Spasova, L. M. Liz-Marzán and M. Farle, Composite silica spheres with magnetic and luminescent functionalities, *Adv. Funct. Mater.*, **16**, 509, 2006.
- [15] N. Insin, J. B. Tracy, H. Lee, J. P. Zimmer, R. M. Westervelt and M. Bawendi, Incorporation of iron oxide nanoparticles and quantum dots into silica microspheres, *ACS Nano*, **2**, 197, 2008.
- [16] S. P. Foy, R. L. Manthe, S. T. Foy, S. Dimitrijevic, N. Krishnamurthy and V. Labhasetwar, Optical imaging and magnetic field targeting of magnetic nanoparticles in tumors, *ACS Nano*, **4**, 5217, 2010.
- [17] J. Berezovsky, M. H. Mikkelsen, N. G. Stoltz, L. A. Coldren, and D. D. Awschalom, Picosecond coherent optical manipulation of a single electron spin in a quantum dot, *Science*, **320**, 349, 2008.
- [18] F. Brochard and P. G. de Gennes, Theory of magnetic suspensions in liquid crystals, *J. Phys. (Paris)*, **31**, 691, 1970.
- [19] S. V. Burylov and Y. L. Raikher, Magnetic Fredericksz transition in a ferronematic, *J. Magn. Magn. Mater.*, **122**, 62, 1993.
- [20] K. I. Morozov, *Phys. Rev. E*, **660**, 11704, 2002.
- [21] V. Berejnov, J.-C. Bacri, V. Cabuil, R. Perzynski, and Yu. Raikher, *Europhys. Lett.* **41**, 507, 1998.
- [22] M. Goryca, P. Plochocka, T. Kazimierzczuk, P. Wojnar, G. Karczewski, J. A. Gaj, M. Potemski, and P. Kossacki, *Phys. Rev. B.*, **82**, 165323, 2010.
- [23] J. E. Tengood, I. S. Alferiev, K. Zhang, I. Fishbein, R. J. Levy, M. Chorny, Brightening of dark excitons in a single CdTe quantum dot containing a single Mn²⁺ ion, *Proc. Natl. Acad. Sci.*, **111**, 4245, 2014.
- [24] K. Sato, Measurement of magneto-optical Kerr effect using piezo-birefringent modulator, *Jpn. J. Appl. Phys.*, **20**, 2403, 1981.

Chapter 5 references

- [1] B. Issa, I. M. Obaidat, B. A. Albiss, Y. Haik. Magnetic Nanoparticles: Surface Effects and Properties Related to Biomedicine Applications. *Int. J. Mol. Sci.*, **14 (11)**, 21266-21305, 2013.
- [2] M. Arruebo, R. Fernández-Pacheco, M. R. Ibarra, J. Santamaría. Magnetic nanoparticles for drug delivery. *Nano Today*, **2 (3)**, 22-32, 2007.
(<http://www.sciencedirect.com/science/article/pii/S1748013207700841>)
- [3] S. R. Cherry, A. Y. Louie, R. E. Jacobs. The Integration of Positron Emission Tomography with Magnetic Resonance Imaging. *Proceedings of the IEEE*, **96**, 416, 2008.
- [4] K. Y. Win, S-S Feng. Effects of particle size and surface coating on cellular uptake of polymeric nanoparticles for oral delivery of anticancer drugs. *Biomaterials*, **26 (15)**, 2713-2722, 2005.
- [5] M. T. Quint, S. Delgado, J. H. Paredes, Z. S. Nuno, L. S. Hirst, and S. Ghosh. All-optical switching of nematic liquid crystal films driven by localized surface plasmons. *Opt. Express*, **23**, 6888-6895, 2015.
- [6] A. N. Shipway, E. Katz, I. Willner. Nanoparticles Arrays on Surfaces for Electronic, Optical, and Sensor Applications. *ChemPhysChem*, **1**, 18-52, 2000.
- [7] Z. Chen, J. Moore, G. Radtke, H. Siringhaus, S. O'Brien. Binary Nanoparticle Superlattices in the Semiconductor-Semiconductor System: CdTe and CdSe. *J. Am. Chem. Soc.*, **129 (50)**, 15702-15709, 2007.
- [8] S. V. Burylov and Y. L. Raikher, Magnetic Fredericksz transition in a ferronematic, *J. Magn. Magn. Mater.*, **122**, 62, 1993.

- [9] J. J. Amaral, J. Wan, A. L. Rodarte, C. Ferr , M. T. Quint , R. J. Pandolfi, M. Scheibner, L. S. Hirst, S. Ghosh. Magnetic field induced quantum dot brightening in liquid crystal synergized magnetic and semiconducting nanoparticle composite assemblies. *Soft Matter*, **11**, 255-260, 2015.
- [10] A. G. del Aguila, G. Pettinari, E. Groeneveld, C. de Mello Donegá, D. Vanmaekelbergh, J. C. Maan, and P. C. M. Christianen. Optical Spectroscopy of Dark and Bright Excitons in CdSe Nanocrystals in High Magnetic Fields. *The Journal of Physical Chemistry C*. (Just Accepted Manuscript) 2017.